ORIGINAL PAPER

Experimental exploration of polycyclic aromatic hydrocarbons stability in subduction zones

Laurie Besognet[1] · Baptiste Debret[1] · Julien Siebert[1] · Nicolas Wehr[1] · Alain Brunelle[2] · Bénédicte Ménez[1]

Abstract

Thermodynamic, experimental and field studies have suggested that organic compounds could be stable, and in some cases predominate over inorganic carbon species, within subduction zones under high pressure and high temperature (HP-HT) conditions. Beyond sedimentary organic matter of biological origin, solid organics can be inherited from hydrothermal circulation at mid-ocean ridges or abiotically formed by carbonate destabilization in the slab. To assess the fate of solid organic compounds during subduction, HP-HT experiments using piston-cylinder and multi-anvil presses have been performed at 700–1000 °C and 3–7 GPa. Different starting solids were tested, including either synthetic polycyclic aromatic hydrocarbons (PAHs) alone, with (i.e., 1-hydroxypyrene, 1-pyrenebutyric acid) or without (pyrene) oxygen-bearing functional groups, or a mixing of pyrene and antigorite. Our results show that increasing P–T conditions lead to the formation of hydrogenated (±oxygenated) graphitic carbon preserving a high level of structural disorder, far from graphite structure. We also observe the formation of aqueous fluids during experiments at 700 °C and 3 GPa with oxygen-functionalized PAHs, suggesting quick water release from solid organic compounds at HP-HT in subduction zones. Pyrene-antigorite experiments reveal various mineral assemblages depending on redox conditions. Oxidizing conditions favor the formation of magnesite-enstatite-coesite while reducing conditions promote forsterite-enstatite-graphitic carbon assemblages. Our results finally highlight the limited reactivity of solid organic compounds when exposed to aqueous fluids derived from serpentinite under reducing conditions which could facilitate the recycling of organic carbon into the deep mantle.

Keywords Deep carbon cycle · Polycyclic aromatic hydrocarbons · Subduction · Experimental petrology

Introduction

The deep carbon cycling has been the subject of intense controversies over the last decade (e.g., Dasgupta and Hirschmann 2010; Kelemen and Manning 2015; Plank and Manning 2019). Among the parameters governing carbon transfer between Earth reservoirs, redox conditions (i.e., oxygen fugacity, fO_2) exert major control over carbon speciation (from C(−IV) in methane CH_4 to C(+IV) in carbon dioxide CO_2, a redox range covering inorganic and organic carbon species) and mobility in fluids at high pressure-high temperature (HP-HT; Sverjensky et al. 2014; Guild and Shock 2020; Bouilhol et al. 2022). Solid carbonates are the main carbon pool entering subduction zones (Dasgupta and Hirschmann 2010; Kelemen and Manning 2015; Plank and Manning 2019) and thus carbonate stability and dissolution in HP metamorphic fluids are relatively well studied (e.g., Gorman et al. 2006; Manning et al. 2013; Pan et al. 2013; Ague and Nicolescu 2014; Facq et al. 2014; Menzel et al. 2020; Farsang et al. 2021). Conversely, not much is conclusively known about the fate of solid organic compounds (i.e., rock-hosted compounds with C-H bonds) during slab evolution, including dehydration, at HP-HT.

Up to now, the main solid organic pool considered in deep carbon flux models (e.g., Plank and Manning 2019) is biological organic matter in oceanic sediments. Yet solid organic compounds of abiotic origin are now increasingly found in the oceanic lithosphere, resulting from magmatic

✉ Laurie Besognet
   besognet@ipgp.fr

1   Université Paris Cité, Institut de Physique du Globe de Paris, CNRS, 75005 Paris, France

2   Laboratoire d'Archéologie Moléculaire Et Structurale, LAMS, CNRS, Sorbonne Université, 4 place Jussieu, Paris, France

degassing and/or hydrothermal circulation along the ridge system (Sforna et al. 2018; Andreani and Ménez 2019; Andreani et al. 2023) or (HP-HT) reactions during subduction (Galvez et al. 2013; Vitale Brovarone et al. 2017; Nan et al. 2020; Bouilhol et al. 2022; Debret et al. 2022; Caurant et al. 2023). The reported condensed carbonaceous matter (CCM), also often referred to as graphitic carbon, consists in a disordered macromolecular structure of high molecular weight composed of variously-functionalized and polymerized aromatic and aliphatic moieties. Under hydrothermal conditions, CCM formation is described in olivine-rich igneous rocks and serpentinites formed at (ultra)slow-spreading oceanic ridges (such as in the Northern Appenines ophiolite and at the Mid-Atlantic ridge, as reported by Andreani and Ménez 2019, Sforna et al. 2018 and Andreani et al. 2023) or near forearc trenches (such as the Yap Trench in the western Pacific Ocean as reported by Nan et al. 2020). Its formation is connected to (1) cooling of magmatic fluids leading to carbon re-speciation at mid-ocean ridges or (2) low temperature hydrothermal alteration of ferrous-iron bearing minerals, leading to hydrogen production and subsequent organic synthesis either at mid-ocean ridges and subduction zones (Milesi et al. 2016; Sforna et al. 2018; Nan et al. 2020; Andreani et al. 2023). Abiotic organic synthesis has also been shown to occur at HP-HT conditions during subduction as a consequence of carbonate destabilization and/or metamorphic reactions in an increasing number of studies (Malvoisin et al. 2012; Galvez et al. 2013; Vitale Brovarone et al. 2017; Tao et al. 2018; Bouilhol et al. 2022; Debret et al. 2022; Caurant et al. 2023). In addition to nano- to micro-diamonds, a wide variety of solid organic compounds is observed in this setting including amorphous carbon, graphitic carbon (also referred to as nano/microcrystalline graphite, graphite-like or simply graphite) but also hydrocarbons. Recently, functional groups typical of organic acids have also been reported along with amorphous carbon, as coating the surface of diamonds hosted in fluid inclusions (Frezzotti 2019). However, our understanding of solid organic compound stability, their mechanism of formation as well as their role in the deep carbon cycle remains limited, resulting in a major knowledge gap.

A growing body of literature tackles the question of the stability of (abiotic) organic compounds in metamorphic fluids at HP-HT using thermodynamic calculations or experiments. Manning et al. (2013) first calculate the solubility of pure graphite in subduction fluids. They show that graphite could be easily dissolved, especially in CO_2-rich-fluids at HP-HT (i.e., at 0.2 GPa and 1000 °C), conversely to what was previously thought based on its refractory character. This result is confirmed experimentally by Tumiati et al. (2020), who study the solubility of graphite and amorphous carbon (glass-like carbon) in HP-HT fluids through piston-cylinder (PC) redox-buffered experiments conducted

at pressures ranging from 1 to 3 GPa and temperatures of 800 °C. Pure glass-like carbon is used in their study as an analogue for disordered carbonaceous matter of biological origin. They report an enhanced dissolution of glass-like carbon compared to crystalline graphite, declining at increasing pressure. Above 3.4 GPa at 800°C, glass-like carbon could be less soluble than graphite. Therefore, they speculate that, alternatively to graphite and even diamond, disordered carbonaceous matter should be the stable carbon polymorph. This study highlights how "intermediate" solid organic compounds with a redox state comprised between those of methane and pure graphite (C(0)), should be considered in subduction zones due to their specific properties including solubility and stability, among others. Along the same lines, Sverjensky et al. (2014) thermodynamically predict the composition of fluids at equilibrium with eclogitic and peridotite minerals (i.e., for temperature between 600 and 900 °C and pressure of 5.0 GPa). They conclude for eclogitic minerals that dissolved organic acids such as acetate (CH_3COO^-) and propionate ($CH_3CH_2COO^-$) can dominate over carbonate species and methane in HP-HT fluids, depending on fO_2 and pH values. Stability of a Mg_silicate/propionate complex ($Mg[OSi(OH_3)][CH_3CH_2COO]$) was also predicted at 1 GPa and 800 °C from experimental data and thermodynamic calculations (Tumiati et al. 2017; Tiraboschi et al. 2018).

Similarly, Huang et al. (2017) explore the stability of acetate ions at 300 °C and 2.4–3.5 GPa in diamond anvil cell (DAC) experiments and show the formation in water of immiscible hydrocarbons coexisting with carbonate crystals. Szlachta et al. (2022) further test the stability of acetate up to 5 GPa and 600 °C, also using sodium acetate aqueous solutions. They observe the decomposition of acetate into hydrocarbons and solid carbonaceous matter beyond 4 GPa and 500 °C. Huang et al. (2023) perform DAC experiments using calcium acetate $Ca(CH_3COO)_2$ aqueous solutions as starting material and report the formation of hydrocarbons, carbonate CO_3^{2-} and bicarbonate HCO_3^- ions and $CaCO_3$ crystals (i.e., calcite or aragonite). Finally, Li (2016) shows the formation of hydrocarbons from sodium acetate aqueous solutions in synthetic fluid inclusions trapped in quartz crystal at 1.5–2.5 GPa and 600–700 °C, in the presence of different mineral redox buffers. Graphitic carbon (referred to as graphite in the study) formation is also reported in these experiments when buffered by nickel-nickel oxide Ni-NiO (NNO), cobalt-cobalt oxide Co-CoO and rhenium-rhenium oxide Re-ReO$_2$ (RRO). It is interesting to note that, although these studies focus on dissolved carbon species, they also report the formation of solid organic compounds, i.e., graphitic carbon. The later are unfortunately often poorly characterized in these studies.

While natural abiotic solid organic compounds have not yet been studied experimentally at HP-HT, the stability of solid organic compounds of biological origin was

already investigated in sedimentary or subduction context. For example, kerogen stability was examined at increasing pressure and temperature in order to characterize the thermal maturation and graphitization of sedimentary organic matter (up to 1450 °C and 8 GPa; Ross et al. 1991; Bustin 1995; Beyssac et al. 2003; Zeng and Wu 2007; Nakamura et al. 2017; 2020). During these experiments, as expected from comparison with natural systems, kerogens evolve chemically and structurally from an amorphous macromolecular carbon structure with hydrogen and heteroatoms (including O, N, and S) to graphite or graphitic carbon depending on the graphitizable or non-graphitizable nature of the studied kerogen (Buseck and Beyssac 2014). This graphitizable character depend on chemical composition and the structure of the kerogen precursor (hydrogen-rich with predominantly long chain aliphatic structures vs. oxygen-rich with high content of cyclic and aromatic structures) and refers to the possibility to synthetize graphite after additional laboratory heat treatment (without pressure). Even at very high temperature, kerogens derived from oxygen-rich, strongly aromatic and cyclic precursors are non-graphitizable, leading to graphitic carbon with increasing temperature and not graphite. This contrasts with natural settings where, even if the associated kinetics are very slow, all biological solid organic compounds are converted to crystalline graphite over 700 °C thanks to hydrostatic pressure and geological timescales (Beyssac et al. 2002; Buseck and Beyssac 2014). Immature and non-graphitizable kerogens (often attributed to Type III or Type IV kerogens, rich in O and S, respectively) share some structural and chemical similarities with abiotic CCM, especially in terms of aromaticity degree, aliphaticity and heteroatom contents and could be regarded as analogues to run HP-HT experiments aiming at characterizing CCM stability. However, natural kerogens can be highly heterogeneous in chemical structure and composition depending on their biological precursors, conditions of formation and thermal maturation. As the chemistry and structure of abiotic CCM are not yet well constrained, it is accordingly difficult to find a kerogen that constitutes a relevant analogue. Moreover, the host rock of kerogen (i.e., sediments) differs from the magmatic one of CCM, which is often found spatially related to (hydrated) mantle mineral, e.g., serpentine, olivine. The host rock could have an influence on the evolution of CCM for instance via the iron content capable of interacting with other redox-sensitive elements and compounds, or via the catalytic properties of certain rock-forming minerals known to have an impact on abiotic organic synthesis. Natural observations (e.g., Debret et al. 2022; Bouilhol et al. 2022) of HP-serpentinites highlight a wide range of structural and compositional diversity of solid organic compounds, which is not observed in eclogitic meta-sediments in similar settings. The host rock could

therefore impact the synthesis pathways and thermal evolution of solid organic compounds during subduction. The host rock is even reported to affect the analysis of organic matter, as highlighted by Matthewman et al. (2013) for meteorites with comparable paragenesis.

To avoid possible biases in using inappropriate kerogen references in HP-HT experiments or numerical modelling, polycyclic aromatic hydrocarbons (PAHs) could represent better analogues of abiotic solid organic compounds. PAHs (e.g., naphthalene $C_{10}H_8$, anthracene $C_{14}H_{10}$, pyrene $C_{16}H_{10}$) which are composed of multiple aromatic rings have already been used in this purpose in thermodynamic calculations (Milesi et al. 2016; Andreani et al. 2023). PAHs stability was also experimentally studied at HP-HT conditions by Chanyshev et al. (2015, 2017a; b) and Davydov et al. (2004). These authors conducted experiments using powdered solid PAHs from 1.3 to 8.0 GPa and up to 1300 °C in which they report PAHs turning into graphitic carbon by dehydrogenation and condensation reactions. However, the potential role of slab minerals on the reactivity of these compounds (e.g., during slab dehydration) has not been yet investigated experimentally, as is the HP-HT stability of more diverse and complex PAHs including functionalized ones. Until now, PAHs and serpentine mixing has only been studied from a planetary accretion perspective via shock pressure experiments (in the range 6–37 GPa; Mimura et al. 2005). Here, we examine the fate of CCM during subduction using HP-HT experiments along a subduction gradient (i.e., 700–1000 °C, 3–7 GPa) involving either a PC press or a multi-anvil press (MAP). We investigate different CCM analogues, including pyrene and oxygen-functionalized PAHs (i.e., 1-hydroxypyrene $C_{16}H_9$-OH and 1-pyrenebutyric acid $C_{16}H_9$–CH_2–CH_2–CH_2-COOH, which contain alcohol or carboxylic groups, respectively), to better match CCM chemical structure and composition observed at mid-ocean ridges. These solid organic compounds were used alone or, in the case of pyrene, mixed with HP serpentine (i.e., antigorite). We observe for all PAH types that the increase in pressure and temperature leads to the formation of hydrogenated (±oxygenated) graphitic carbon with a preserved structural disorder, thereby allowing the transport of carbon and volatiles into the deep Earth. The release of aqueous fluids from organics is observed with 1-pyrenebutyric acid at 3 GPa and 700 °C. Concerning the stability of pyrene during serpentinite dehydration (i.e., antigorite and chlorite breakdown), we show that various assemblages are stabilized in the used HP-HT devices. This is likely explained by the variable redox conditions imposed by different experimental assemblies, which appear as the primary factor controlling the form and mobility of carbon in subduction settings.

Material and methods

Polycyclic aromatic hydrocarbons and natural antigorite samples

Four series of experiments were conducted using different starting materials (Table 1). The first three experiment series used PAHs purchased from Sigma Aldrich, namely pyrene (sublimed grade, 99% purity), 1-hydroxypyrene (purity > 97%) and 1-pyrenebutyric acid (purity > 97%, hereafter to as PyBA). The synthetic PAHs were ground to powder using agate mortar and pestle and then loaded in platinum (Pt) capsules for HP-HT experiments.

The fourth series of experiments used a 50:50 mixing (by mass) of pyrene and natural antigorite powders. Antigorite came from a natural sample, i.e., Vis-9, from the Monviso meta-ophiolite (Debret 2013). To avoid weathered surface, the inner part of the field rock specimen was cut with a copper saw blade before being ultrasonically cleaned in an absolute ethanol bath and then ground using agate mortar and pestle. During grinding, as much grains as possible of opaque mineral phases (i.e., iron sulfides and magnetite) were removed by hand in order to obtain the purest possible antigorite powder.

Major element and volatile composition of the powdered antigorite was analysed at the Service d'Analyses des Roches et des Minéraux (SARM, Nancy, France; Table 2) by inductively coupled plasma optical emission spectroscopy (ICP-OES, Thermo Scientific iCAP 6500). Sample digestions for major element analysis (i.e., SiO_2, Al_2O_3, Fe_2O_3, MnO, MgO, CaO, Na_2O, K_2O, TiO_2, P_2O_5) were performed on $LiBO_2$ fluxed fusions following the procedure described by Carignan et al. (2001). The standard reproducibility was better than 2% for major elements based on repeated analyses of the UB-N serpentinite standard from the Centre de Recherches Pétrographiques et Géochimiques (CRPG, Nancy, France). Whole rock sulfur and carbon contents were determined on a carbon–sulfur (CS) analyser Leco SC144 DRPC by the SARM. This involved high temperature combustion of 250 mg of powdered rock sample and infrared detection of effluents. The analyses were below detection limit (<0.01%), showing the absence of detectable impurities such as sulfur and carbon phases in the powdered antigorite. Iron redox state in antigorite was determined first by X-ray absorption spectroscopy (XAS) at the iron K-edge at the LUCIA beamline of SOLEIL synchrotron (Source Optimisée de Lumière d'Energie Intermédiaire du LURE, Saint Aubin, France) on antigorite minerals in the field sample thin sections giving a $Fe^{3+}/\Sigma Fe$ of 0.2 (with ΣFe corresponding to the total Fe^{2+} and Fe^{3+}). Automatic titration at the SARM on the powdered antigorite (from which magnetite crystals were handpicked) gives an identical ratio $Fe^{3+}/\Sigma Fe$ of 0.2 (Supplementary Methods). As both the low FeO content (Table 2) and $Fe^{3+}/\Sigma Fe$ estimates from bulk analysis of the powdered antigorite are consistent with in situ analyses on antigorite minerals, this suggests the absence of magnetite (or other Fe-bearing accessory phases) in the powdered antigorite used for experiments. This is also consistent with petrographic observation which reveals the quasi absence of magnetite in the hand specimen (Debret 2013). The powdered antigorite (between 2 and 15 mg, depending on the experiment) was mixed with the powdered pyrene and introduced in the Pt capsules for HP-HT experiments.

High pressure experiments

The experiments were performed at Institut de physique du globe de Paris (IPGP, Paris, France) using either an end-loaded PC press or a Walker-type MAP. The PC press was favoured for low P conditions (i.e., antigorite breakdown, in chlorite stability field; Fig. 1) while the MAP was used for higher P–T conditions (i.e., chlorite breakdown, in garnet and diamond stability fields; Fig. 1). To investigate kinetic effects, various run durations were tested for the pyrene series (i.e., 1. 2. 3 and 7 days based on literature review) while the other series were run during 72 h. The pressure and temperature conditions, also reported in Fig. 1, duration of the experiments and a summary of the starting materials and run products are given in Table 1. The starting materials were encapsulated as a homogeneous powder into Pt tubes. Platinum was chosen for its non-reactivity with the starting compounds (organic matter or silicates) in the chosen P–T conditions (see Jakobsson 2012 who discusses Pt permeability for carbon). The capsules were welded on both sides with dimensions ranging from 1.8 to 7.6 mm in length and 1.6 to 2.0 mm in outer diameter, depending on the type of press and the experiment. For the PC experiments, we used a standard ½″ assemblage with talc-Pyrex pressure medium, a graphite furnace and fired magnesia MgO spacers (e.g., Blanchard et al. 2015; see Supplementary Fig. S1). The temperature was monitored using a tungsten-rhenium W–Re thermocouple (type D, W-3% Re/W-25% Re) passing through a four holes alumina Al_2O_3 tube. For the MAP experiments, a 10/5 type assemblage was used, including a MgO octahedron, a lanthanum chromite $LaCrO_3$ insulating sleeve, a Re furnace, MgO spacers, a zirconia disk Zr_2O for thermal insulation and an alumina disk isolating the Pt capsule from the W–Re thermocouple (e.g., Siebert et al. 2011; see Supplementary Fig. S1). The thermocouple is guided by an alumina tube. These experiments were performed with a heating rate of about 100 °C min^{-1}, and quenching was achieved by turning off the furnace power. It is important to note that the utilization of different furnaces is believed to have an impact on the redox stability of silicates and opaque

Table 1 Experimental conditions with starting material and solid products, and Raman parameters of the D and G bands obtained for the produced graphitic carbon

| Starting material, conditions and run products | | | | | Raman D and G bands parameters | | | | | | | R1 |
	P (GPa)	T (°C)	Duration (h)	Run products	G (cm⁻¹)	D1 (cm⁻¹)	D2 (cm⁻¹)	D3 (cm⁻¹)	RBS (cm⁻¹)	G-FWHM (cm⁻¹)	D1-FWHM (cm⁻¹)	
Pyrene												
PC1e	3	700	24	CGr	1600	1348	x	x	252	53	56	1.57
PC1d	3	700	48	CGr	1599	1347	x	x	252	52	56	1.54
PC1f	3	700	72	CGr	1598	1348	x	x	251	54	56	1.60
PC1b	3	700	168	CGr	1598	1348	x	x	250	56	51	1.88
PC1c	3	1000	72	CGr	1583	1355	1623	x	228	22	30	0.65
MAP1a	7	1000	72	CGr	1580	1352	1620	x	228	20	43	0.35
1-Hydroxypyrene												
PC5	3	700	72	CGr	1598	1348	x	x	250	55	56	1.60
MAP5	7	1000	72	CGr	1581	1353	1622	x	228	25	45	0.51
1-Pyrenebutyric acid												
PC4	3	700	72	CGr	1598	1348	x	x	250	55	45	1.69
MAP4	7	1000	72	CGr	1580	1353	1622	x	227	22	44	0.33
Pyrene (50%)/antigorite (50%)												
PC2a	3	700	72	En+Fo+Chl+CGr	1599	1349	x	x	250	55	51	1.95
PC2d	3	700	72	En+Fo+Chl+CGr								
MAP2b	7	700	72	En+Fo+Mgs+Al-bearing phase+CGr	1593	1348	x	1527	245	66	68	1.46
PC2b	3	1000	72	En+Fo+CGr	1581	1355	1623	x	225	23	39	0.19
MAP2a	7	1000	72	En+Prp+Fo+Mgs+CGr	1581	1353	1622	x	228	21	43	0.21
MAP2c	7	1000	72	En+Prp+Coe+Mgs+CGr	1579	1351	1616	1527	228	27	50	0.55
MAP2e	7	1000	72	En+Prp+Fo+Mgs+CGr								

PC experiments (using graphite furnace) have label starting with PC while MAP experiments (using rhenium furnace) have MAP-label. The label number relates to the starting material (1 = pyrene, 2 = pyrene and antigorite, 4 = PyBA, 5 = 1-hydroxypyrene). G, D1, D2 and D3 indicate fitted band positions according to the procedure described in Henry et al. (2019). RBS: Raman band separation between G and D1 fitted band positions (RBS = G − D1), FWHM: full width at half maximum, R1: ratio of fitted band height (D1/G). CGr: graphitic carbon, Chl: chlorite, Coe: coesite, En: enstatite, Fo: forsterite, Mgs: magnesite, Prp: pyrope

Table 2 Composition (in weight %, wt%) of the powdered Monviso antigorite (sample Vis-9) used in pyrene-antigorite (50:50 by mass) experiments

Species	wt%
SiO_2	42.02
Al_2O_3	1.67
$Fe_2O_{3\,tot}$	5.86
MnO	0.10
MgO	38.25
CaO	<D.L.
Na_2O	<D.L.
K_2O	<D.L.
TiO_2	<D.L.
P_2O_5	<D.L.
LOI	11.81
Total	99.72
CO_2 total	<0.01
H_2O	12.22
FeO_{LOI}	4.13
S total	<0.01
C_{org}	<0.01

<D.L. below detection limit
LOI loss on ignition

Fig. 1 Experimental pressure–temperature stability field of antigorite and chlorite and experimental conditions. Thick lines indicate key dehydration reactions, i.e., the antigorite-out (dark green, solid) and the chlorite-out (light green, dashed) from experimental studies. Only selected results are shown. It includes, for antigorite: UT95: Ulmer and Trommsdorff (1995), WS97: Wunder and Schreyer (1997), BN98: Bose and Navrotsky (1998), BP03: Bromiley and Pawley (2003), P10: Padrón-Navarta et al. (2010); for chlorite: FP04: Fumagalli (2004), FP14: Fumagalli et al. (2014). Stars and polygons represent the experimental conditions used with the PC press (in the range 3 GPa and 700–1000 °C) and the MAP (in the range 7 GPa and 700–1000 °C), respectively. Slab surface P–T paths modelled by Syracuse et al. (2010) are shown using coloured arrows, with an average path for cold and hot subduction in blue and red, respectively. Graphite-diamond and quartz–coesite transitions are represented by dashed lines. Atg: antigorite, Chl: chlorite, Grt: garnet, Ol: olivine, Opx: orthopyroxene, PhA = phase A, Ta = talc

phases during serpentine dehydration experiments (Maurice et al. 2020), as further discussed.

Characterization of run products

After quench and decompression of the experiments, the capsules were embedded in KM-U resin (Presi), hand polished with silicon carbide abrasion papers (SiC; 15.3, 10 and 5 µm grain size) and absolute ethanol until the experimental material outcrops and finally cleaned in an absolute ethanol ultrasonic bath.

Raman spectroscopy

Raman analyses were performed at IPGP with a Renishaw In Via Raman spectrometer coupled to an Olympus BX61 microscope, using the 514 nm wavelength of an argon ionized laser (HÜBNER Photonics) dispersed by a holographic grating of 1800 grooves mm^{-1}. The measurements were performed with a 50× objective (numerical aperture: 0.75), a configuration allowing to obtain a planar resolution close to 1 µm. The calibration of Raman bands was performed before each measurement session using a silicon microprocessor chip with a characteristic band at 520.4 cm^{-1}. Spectra were collected in the range of 130–4000 cm^{-1} using a Renishaw CDD camera for punctual analysis. The laser power varied between 0.25, 2.5 and 12.5 mW, depending on the fluorescence level, the nature of the probed material (minerals vs. graphitic carbon) and the associated signal to noise ratio. For graphitic carb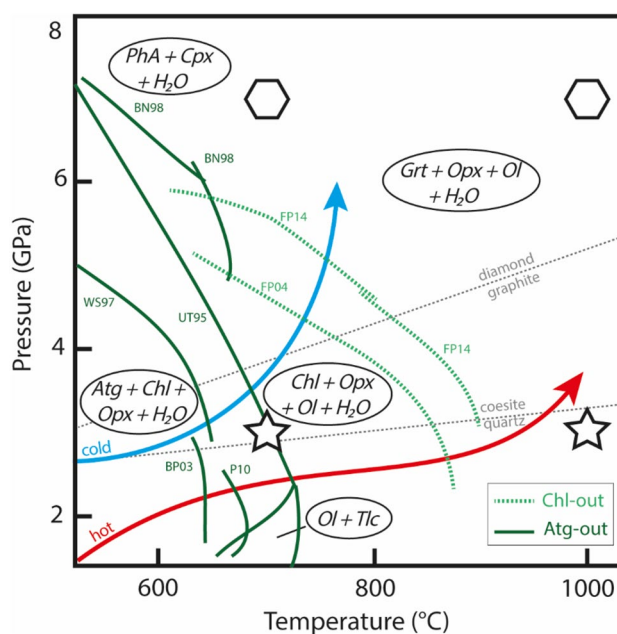on analyses the power was set to the minimal value in order to avoid any radiation damage. Acquisition time was set to 10 s and each spectrum corresponds to 2 cumulative 10 s cycles. Each graphitic carbon spectrum presented in figures is an average of 5 spectra collected on identical compounds. The baseline of the spectra were realized with Peakfit 4.0 software (Jandel Scientific) over the 1000–1800 cm^{-1} region, considering a cubic function. Deconvolution of bands characteristic of graphitic carbon was performed with the Wire 5.4 software (Renishaw).

Graphitic carbon Raman spectra can be decomposed into two regions, named first and second order regions (see Henry et al. 2019 for a review). The first order region, ranging between 1000 and 1800 cm^{-1}, is composed of two main bands D and G at about 1350 and 1580 cm^{-1}, respectively. The G band (for graphite) is related to the in-plane stretching vibration of carbon atoms in an aromatic ring with E_{2g} symmetry; this is the only band present in pure graphite. The

D band (for defect), also called D1, is the result of structural and chemical defects in graphitic carbon, precisely the breathing motion of sp^2 C atoms in an aromatic ring with a A_{1g} symmetry (Tuinstra and Koenig 1970). In graphitic carbon, there are additional minor bands, also due to disorder, namely D2 (at about 1610 cm^{-1}), D3 (at about 1500 cm^{-1}), D4 (at about 1200 cm^{-1}), D5 (at about 1260 cm^{-1}) and D6 (at about 1440 cm^{-1}). The detailed interpretation of these additional bands D2, D3, D4, D5 and D6 is reviewed by Henry et al. (2019). Briefly, the D2 band is related to the presence of disorder in an aromatic ring with E_{2g} symmetry. The D3 band is related to out-of-plane vibration due to chemical defects. The D4 and D5 bands are linked to C-H moieties in aliphatic hydrocarbons, as is presumably the D6 band. The most visible of these bands is D2, which nonetheless overlaps with the G band in the case of low graphitization degree but becomes more distinct as the graphitization degree increases and the G band shifts to lower wavelengths.

The second order region, between 2400 and 3400 cm^{-1}, is composed of four bands S1, S2, S3 and S4 at about 2450, 2700, 2900 and 3180 cm^{-1}, respectively. The second order region is interpreted as overtones and combinations of the bands of the first order region (Beyssac et al. 2002; Wopenka and Pasteris 1993). For instance, the S2 band at 2700 cm^{-1} is an overtone of the D-band at 1350 cm^{-1}.

The Raman spectra of graphitic carbon evolve with increasing crystallinity, until reaching the graphite structure. Especially, in the first order region, during graphitization, the D band shifts toward higher wavelengths, sharpens and increases in intensity to exceed the G band intensity by a factor of two before finally decreasing and disappearing upon pure graphite formation. The G-band shifts toward lower wavelengths, thickens a little before sharpening and increasing until it becomes the only visible band (Buseck and Beyssac 2014). In the second order region, at low crystallinity, there is a single broad band which disassembles as graphitization proceeds in S2, S3 and S4 bands. With the increase in crystallinity, S2 band is more intense than S3 and S4 and another small band S1 appears. In graphite, S2 band is split into two separate bands G′1 (at 2690 cm^{-1}) and G′2 (at 2735 cm^{-1}).

The deconvolution of first-order region allows to derive different parameters for monitoring the level of graphitization. Here, only G, D1, D2 and D3 bands have been deconvoluted using a Gaussian Lorentzian mixed function. The parameters used in this study are the following:

– D and G band separation value in cm^{-1} (RBS with RBS = G-band position − D1-band position). RBS value is expected to decrease as the graphitization level increases.
– G and D1 band widths (i.e., full width at half maximum, FWHM). Upon graphitization, the D1-FWHM

is decreasing while the G band is gently increasing in intensity before decreasing.
– D1 and G bands height ratio (R1 with R1 = D1 intensity/G intensity). During graphitization, R1 increases until D1 band is about twice more intense than G, then it decreases.

Polishing of the sample is known to increase graphitic carbon D-band intensity and have a controversial effect on its G-band (see Henry et al. 2019 for review) in graphitic carbon. However, such effects seem to be reduced when using abrasion paper (Pasteris 1989) rather than diamond-bearing polishing solutions. To further investigate potential artefacts during polishing, Raman analysis was carried out on one sample (PC1d) unpolished and polished and gives identical results (Supplementary Fig. S2). We therefore consider polishing effects as minimal.

Scanning electron microscopy

Scanning electron microscopy (SEM) images in backscattered electron (BSE) and secondary electron (SE) modes and energy dispersive X-ray spectroscopy (EDS) analyses were collected at IPGP on carbon coated sample surface using an Auriga 40 Zeiss microscope equipped with a Bruker QUANTAX 200 (125 eV resolution). Analytical conditions were 15 kV accelerating voltage, low or high current intensity (i.e., 1.5 and 3 nA) for imaging or EDS analysis, respectively, and a 8.5 mm working distance. Elemental distributions and images were processed using the ImageJ software (Schneider et al. 2012). Olivine, pyroxene and magnesite X_{Mg} values with $X_{Mg} = (Mg + Fe)/Mg_{tot}$ value were derived from SEM–EDS measurements on run products, along with mineral composition in oxide weight percent (wt%).

Time of flight-secondary ion mass spectrometry

Time-of-flight secondary ion mass spectrometry (TOF–SIMS) measurements were carried out using a TOF–SIMS IV reflectron mass spectrometer (IONTOF GmbH) located at the Laboratoire d'Archéologie Moléculaire et Structurale (Sorbonne Université, CNRS, Paris, France). The instrument is equipped with a bismuth liquid metal ion gun delivering a pulsed beam of Bi_3^+ cluster ions. Primary ions of 25 keV struck the sample at an angle of incidence of 45° and a pulsed current of 0.45 pA, with a repetition rate of 10 kHz. The emitted secondary ions were accelerated to 2 keV (extraction at 2 kV) towards a field-free region and a single-stage reflectron (first-order compensation). Secondary ions ejected from the top few monolayers of the sample surface were post-accelerated to 10 keV before reaching the detector comprising a microchannel plate, scintillator and photomultiplier. The focusing mode

of the ion column ensured a spatial resolution of 2–5 μm and a mass resolution of 5000 (FWHM) at a mass-to-charge ratio (m/z) of 500. A low-energy (~20 eV) electron gun was used between two successive pulses of primary ions for charge compensation with minimum damage to the sample surface. An optical camera in the sample vacuum chamber was used to locate the samples, which were deposited on the sample holder without any treatment or adhesive. Sputtering of the sample surface was first carried out to remove potential contaminants using a pulsed argon Ar_n^+ cluster ion beam of 10 keV energy ($n \sim 2000$, 5 eV per Ar atom) over an area of 500 μm × 500 μm (ion fluence of 3.1×10^{14} ions cm^{-2}). In the center of this area, images of ions in negative and positive polarities were acquired over an m/z range from 0 to 800, in a raster pattern over areas of 200 μm × 200 μm and 128 × 128 pixels (pixel size 1.56 μm × 1.56 μm). Images were recorded with a primary ion fluence of 5.2×10^{11} ions cm^{-2} (45 scans with a cycle time of 100 μs). Data were acquired and processed using SurfaceLab 6.6 software (IONTOF GmbH). Spectra from the total analysis area were extracted. Internal mass calibration was performed using low-mass fragment ion signals from C^+, CH^+, CH_2^+, CH_3^+, C_2^+, $C_2H_3^+$, C_3^+, C_4^+ for the positive ion mode and from C^-, CH^-, CH_2^-, C_2^-, C_3^-, C_4^-, C_4H^- for the negative ion mode. Ion peaks were assigned according to instrument resolution, precision and valence rule. Some surface contaminations of easily ionized elements can occur and induce very intense peaks in the spectra (e.g., Na^+, Mg^+, K^+, Ca^+ in positive polarity spectra). These peaks associated with elements absent from the starting material were not taken into account in the list of the ten most intense peaks used to compare the different experiments.

Thermodynamic calculations

We use a Gibbs free energy minimization strategy (Connolly 2005, 2009) to predict, using PerpleX software, phase equilibria of the experiments. Phase diagrams in the CO_2–SiO_2–MgO–H_2O systems were calculated using the Holland and Powell (1998)'s thermodynamic database (revised in 2002, hp02ver.dat datafile). All the activity-composition (a–X) relationships of the phases are from Holland and Powell (2003) except for antigorite which derives from Padrón-Navarta et al. (2010). Model bulk composition derives from antigorite composition in Table 2, excluding aluminium and iron, considering a 50:50 mixing with pyrene (i.e., in mass amount CO_2: 10.8, SiO_2: 37.1, MgO: 33.7, H_2O: 18.4). The fluid was modelled using the equation of state of Holland and Powell (1991, 1998) and includes CH_4, H_2 and CO_2 species. Other organic compounds were not considered in the thermodynamic modelling as the current thermodynamic database of PerpleX at HP-HT is limited to methane (CH_4) and organic acids in fluids (Sverjensky et al.

2014), while the latter could decompose into solid organic compounds (e.g., Szlachta et al. 2022), for which no thermodynamic database is available.

Results

Evolution of pyrene and oxygen-functionalized PAHs at HP-HT

In order to assess the influence of P–T conditions, three experiments using pyrene as starting material were performed during 3 days with PC press at 700 °C and 3 GPa (PC1f), 1000 °C and 3 GPa (PC1c) and with MAP at 1000 °C and 7 GPa (MAP1a) (Table 1). The pyrene yellow powder originally inserted in the Pt capsule was replaced in the three experiments by a dark grey compact layered material, as shown in SEM (Fig. 2a–d). Raman analyses of run products derived from pyrene at increasing P–T conditions after 3 days are displayed in Fig. 2e. In all the experiments, pyrene turns into graphitic carbon characterized by two marked D and G bands in the first order region (in PC1f, at 1348 and 1598 cm^{-1}), and four bands S1, S2, S3 and S4 in the second order region (in PC1f, only S2, S3 and S4 are visible at 2686, 2937 and 3201 cm^{-1} respectively). All pyrene characteristic Raman bands have been replaced (Supplementary Fig. S3). On the SEM images, it is observed that the increase in P–T conditions impacts the crystallinity of run products, showing a more layered material in PC1c and MAP1a (1000 °C and 3–7 GPa, respectively) compared to PC1f (700 °C–3 GPa). It comes together with the Raman spectra showing a substantial change in both the first and second order regions with increasing temperatures (Fig. 2e). At a constant pressure of 3 GPa, the RBS value decreases from 251 cm^{-1} at 700 °C to 228 cm^{-1} at 1000 °C (Table 1). Similar decrease with increasing temperature in observed for D1 and G band FWHM values (from 56 and 54 cm^{-1} to 30–43 and 20–22 cm^{-1}, respectively) as well as R1 ratio (from 1.60 to 0.35–0.65). S1 band appears in the second order region at 2455 cm^{-1}. Conversely, at a constant temperature of 1000 °C and increasing pressure, few changes in the Raman spectra are observed (Fig. 2e). The RBS value is the same (228 cm^{-1}) in all the experiments while the R1 ratio is only decreasing from 0.65 at 3 GPa to 0.35 at 7 GPa (Table 1). Although there are slight variations in the D1-FWHM values (30 cm^{-1} at 3 GPa vs. 43 cm^{-1} at 7 GPa), the G-FWHM values are comparable in the experiments carried out at constant temperature (20–22 cm^{-1}). The only noticeable change is observed in the second order region, where the intensity of the S2 band at 2707 cm^{-1}, drastically decreases between 3 and 7 GPa (Fig. 2e).

In order to highlight possible kinetic effects, four PC experiments were performed using pyrene as starting
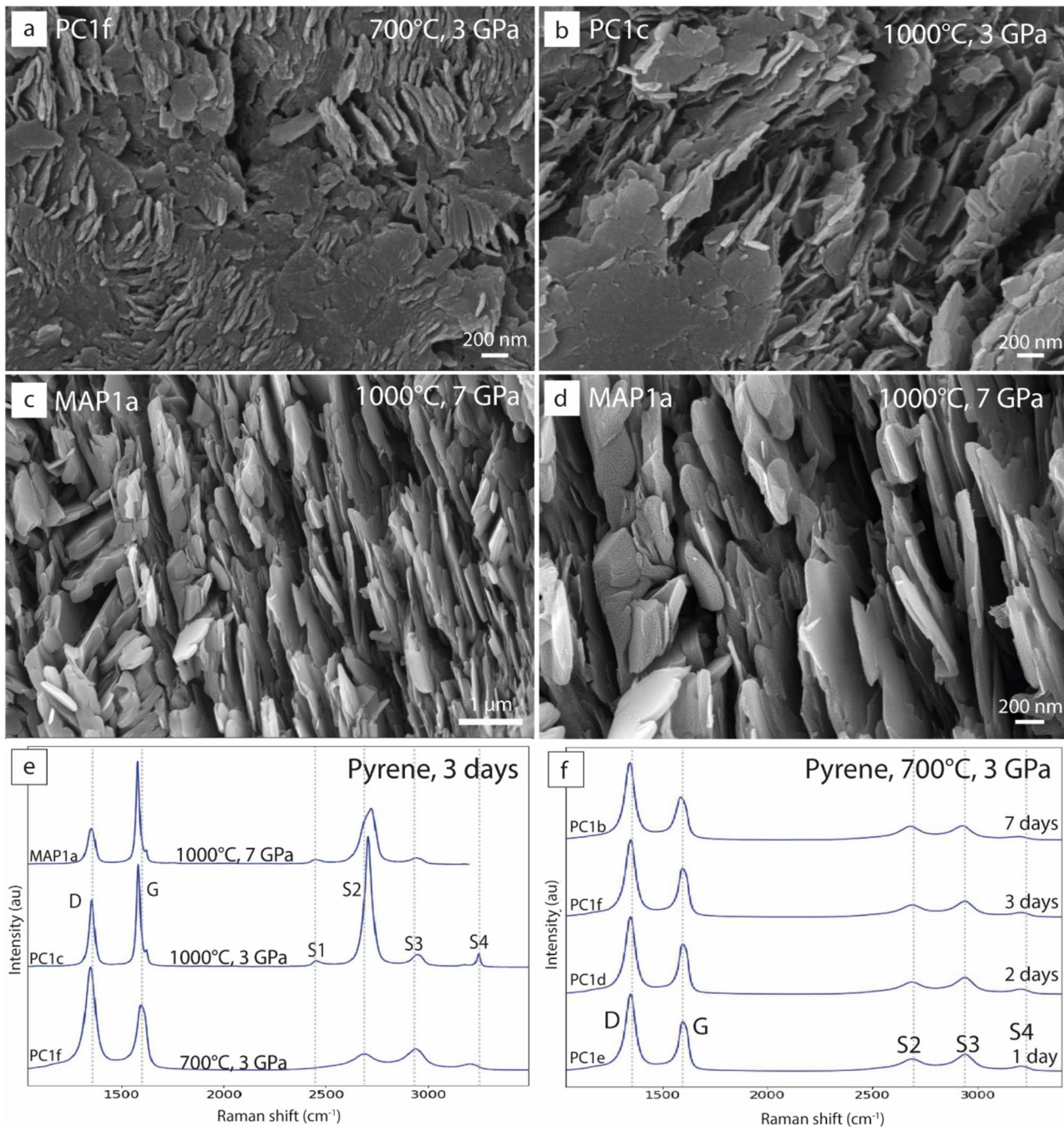
Fig. 2 SEM (secondary electrons, SE) images of experiments performed with pyrene at increasing P and T (PC press and MAP) (**a–d**) and associated Raman spectra (**e, f**). **a** PC1f (700 °C, 3 GPa), **b** PC1c (1000 °C, 3 GPa), **c,d** MAP1a (1000 °C, 7 GPa), **e** pyrene evolution with pressure and temperature for a constant duration of 3 days (i.e., 3 GPa at 700 or 1000 °C (PC press) and 7 GPa at 1000 °C (MAP)). **f** Pyrene evolution with time at constant P and T (i.e., 1, 2, 3 and 7 days at 700 °C and 3 GPa; PC press). Graphitic layers are visible in all experiments, showing higher definition at higher P–T conditions. All collected spectra show the so-called first order D and G bands at ~about 1350 and ~1600 cm^{-1} and the second order S1 to S4 bands in the range 2400–3100 cm^{-1}, all characteristic of graphitic carbon (Henry et al. 2019). Raman D and G band parameters are given in Table 1 together with details on experimental conditions. au: arbitrary unit

material at 700 °C and 3 GPa during 1, 2, 3 and 7 days (PC1e, PC1d, PC1f and PC1b, respectively; Table 1). Raman analyses of run products are displayed in Fig. 2f. In all the experiments, pyrene turns into graphitic carbon characterized by two marked D and G bands in the first order region at about 1348 and 1599 cm^{-1}, respectively, and three bands
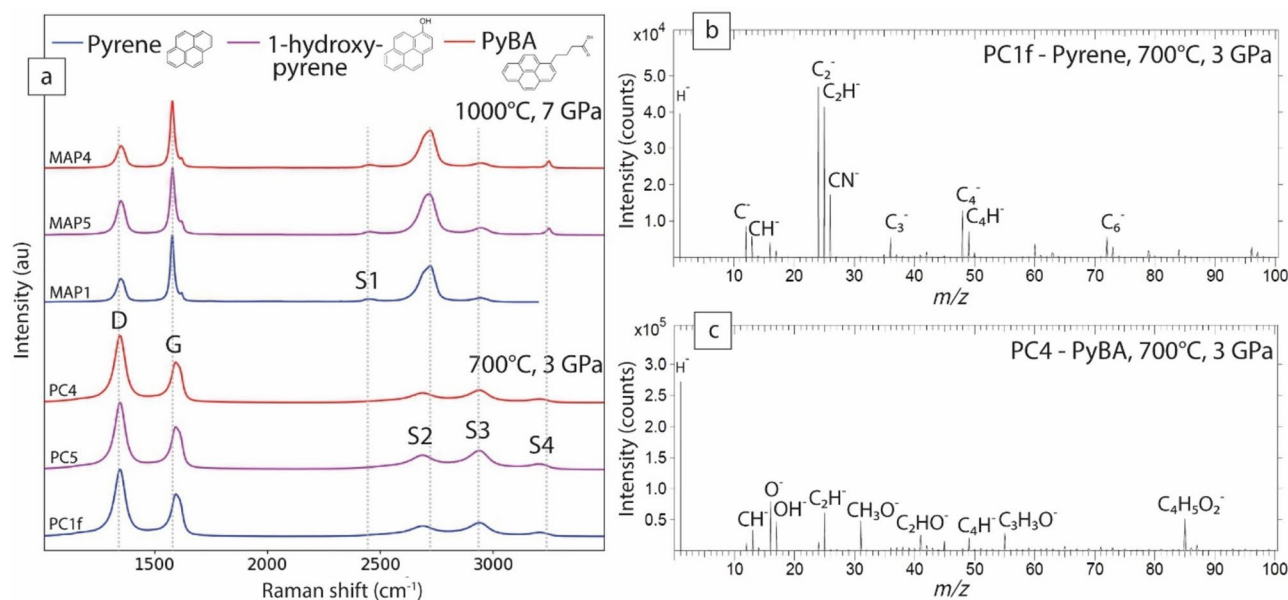
Fig. 3 Raman spectra (**a**) and TOF–SIMS negative polarity spectra (**b**, **c**) collected on run products obtained using PAHs of a single type as starting material in PC press or MAP. **a** Comparison of the evolution of pyrene and two oxygen-functionalized PAHs (1-hydroxypyrene and 1-pyrene butyric acid, PyBA) at 700 °C and 3 GPa (PC) or 1000 °C and 7 GPa (MAP). Raman spectra show graphitic carbon bands that are very similar, indicating an equivalent graphitization level. See Fig. 2 for band assignment and Table 1 for Raman D and G band parameters. **b,c** TOF–SIMS negative polarity spectra (m/z of 0–100) of run products obtained using pyrene (**b**) and PyBA (**c**) at 700 °C and 3 GPa (PC). The first ten most intense fragment ions are indicated (see Supplementary for mass deviation). They are mainly composed of short carbon chains and oxygen-functionalized aliphatic moieties for pyrene and PyBa, respectively. au: arbitrary unit

S2, S3 and S4 in the second order region at about 2686, 2937 and 3201 cm^{-1}. Graphic inspection of Raman spectra shows no substantial change with experiment duration. Systematic deconvolution of the collected spectra shows little variations of G and D1 band parameters (Table 1). The RBS value is about the same in all the experiments (250–252 cm^{-1}). D1-FWHM and G-FWHM values are also comparable between experiments (D1-FWHM = 51–56 cm^{-1}, G-FWHM = 52–56 cm^{-1}). The R1 ratio slightly increases from 1.54 after 2 days to 1.88 after 7 days. However, those variations are not very significant in view of spectra deconvolution error (see also Henry et al. (2019) who reported an error between 5 and 10% for R1 ratio). This overall suggests that equilibrium was reached as early as day 1 and that all experiments performed with PAHs alone can then be considered to be in equilibrium.

To evaluate the effect of PAH functionalization during HP-HT experiments, two series of experiments were conducted for each oxygen-functionalized PAH, at 700 °C, 3 GPa using PC press (PC5 and PC4 for 1-hydroxypyrene and PyBA; respectively) and 1000 °C, 7 GPa using MAP (MAP5 and MAP4 for 1-hydroxypyrene and PyBA, respectively, Table 1; Fig. 3a). SEM observation of the run product derived from 1-hydroxypyrene at 700 °C, 3 GPa shows the same compact aspect as pyrene run product (Fig. 2a). In contrast, for the same P–T conditions, the run product derived from PyBA contains many spherical cavities less than 2 µm wide distributed throughout the material (Fig. 4a) and few larger ones (>10 µm in diameter) (Fig. 4b). The biggest cavities are fractured, relating their formation prior to decompression. TOF–SIMS imaging shows that these textural heterogeneities are also associated with chemical heterogeneities (Fig. 4c), with in particular oxygen-bearing fragment ions $C_3H_3O^+$ preferentially localized in circular shapes and aliphatic fragment ions $C_4H_7^+$ at their periphery in the bulk organic matrix. At 1000 °C and 7 GPa, the run products show for both oxygen-functionalized PAHs the same compact material as pyrene under the same conditions, with very well-defined layers of graphitic carbon (Fig. 2c, d). Associated Raman spectra are compared to those of pyrene in Fig. 3a under the same P–T conditions. Graphic inspection of the spectra shows no discernible differences at both P–T conditions, as confirmed by D1 and G band parameters (Table 1). Indeed, the RBS, R1 and G-FWHM values are very close for the three PAH types for the same P–T conditions (at 700 °C, 3 GPa: RBS = 250 cm^{-1}, R1 = 1.60–1.69, G-FWHM = 54–55 cm^{-1}; at 1000 °C, 7 GPa: RBS = 227–228 cm^{-1}, R1 = 0.33–0.51, G-FWHM = 43–45 cm^{-1}; Table 1), overall indicating similar crystallinity degree of the graphitic carbon obtained in the three experiment series.

TOF–SIMS spectra have been collected on run products obtained from pyrene and PyBA at 700 °C and 3 GPa (PC1f
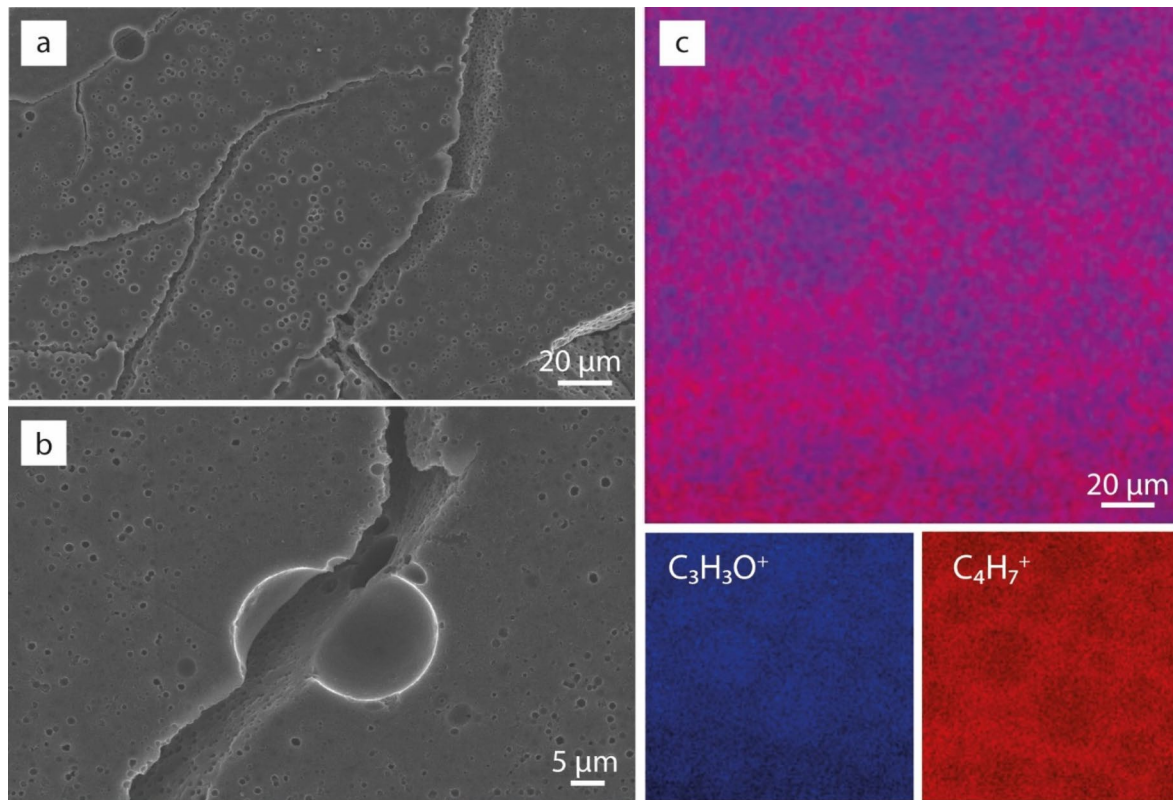
Fig. 4 Chemical and textural heterogeneities in the run product obtained at 700 °C and 3 GPa using PyBA (PC4). **a,b** SEM-SE images of spherical cavities in PC4. Micrometer and tens of micrometer round holes are observable all over the polished capsule. **c** Two-color overlay TOF–SIMS ion images composed of the fragment ions $C_3H_3O^+$ and $C_4H_7^+$ and corresponding individual ion images. Fragment ions are unevenly distributed, with $C_3H_3O^+$ fragment ions preferentially emitted at circular shapes and $C_4H_7^+$ fragment ions at their periphery (see Supplementary Table S1 for mass deviation)

and PC4, respectively). Respective negative polarity spectra over the range $m/z = 0–100$, where most fragment ions have been detected and identified, are shown in Fig. 3b and c (see also Supplementary Table S1). PC1f TOF–SIMS spectrum is mainly composed of short carbon chains (i.e., C^-, C_2^-, C_3^-, C_4^-, C_6^- fragment ions) and aliphatic moieties (i.e., CH^-, C_2H^-, C_4H^- fragment ions). Conversely, PC4 TOF–SIMS spectrum shows mainly oxygen-bearing fragment ions (i.e., O^-, OH^-, CH_3O^- C_2HO^-, $C_3H_3O^-$ $C_4H_5O_2^-$) in addition to short chain aliphatic moieties (i.e., CH^-, C_2H^-, C_4H^-). Similar trends were seen in the positive polarity spectra (Supplementary Fig. S4a–b; Table S1).

Evolution of pyrene and antigorite mixing at HP-HT

To assess the impact of serpentinite dehydration on PAH P–T evolution, seven experiments were conducted using a 50:50 mixing (by mass) of pyrene and natural antigorite powders at temperatures ranging from 700 to 1000 °C and pressure of 3 GPa in PC press (PC2a, PC2d, and PC2b) and from 700 to 1000 °C and 7 GPa in MAP (MAP2b, MAP2a, MAP2c, MAP2e), beyond antigorite and chlorite stability

fields, respectively (Table 1; Fig. 1). In all experiments, the pyrene and antigorite mixing turned into an assemblage of silicate- and graphitic carbon domains of about several hundred micrometers in size (Fig. 5).

At 3 GPa and 700 °C (PC2a and PC2d; Fig. 5a), silicate domains are made of microcrystalline assemblages of pyroxene (i.e., enstatite with X_{Mg} values ranging from 0.94. to 0.95, representing around 20% of the run products visible at the surface of the polished capsule), olivine (forsterite with X_{Mg} values ranging from 0.91 to 0.94; around 20%) and chlorite (close to clinochlore end-member; <10%), as established by SEM–EDS (Supplementary Table S2) and Raman analysis. These assemblages are classic products of antigorite breakdown predicted by thermodynamic calculations or established experimentally (Fig. 1).

At 3 GPa and 1000 °C (PC2b; Fig. 5c), after chlorite breakdown, only the anhydrous silicate phases remain, i.e., enstatite and olivine with X_{Mg} values of 0.93 and 0.95, respectively. Enstatite crystals form lamellae or needles (up to 40 μm in length). No aluminium-rich phase was observed in the quenched experiment. Indeed, the bulk Al_2O_3 content is very low (Supplementary Table S2), so is the expected
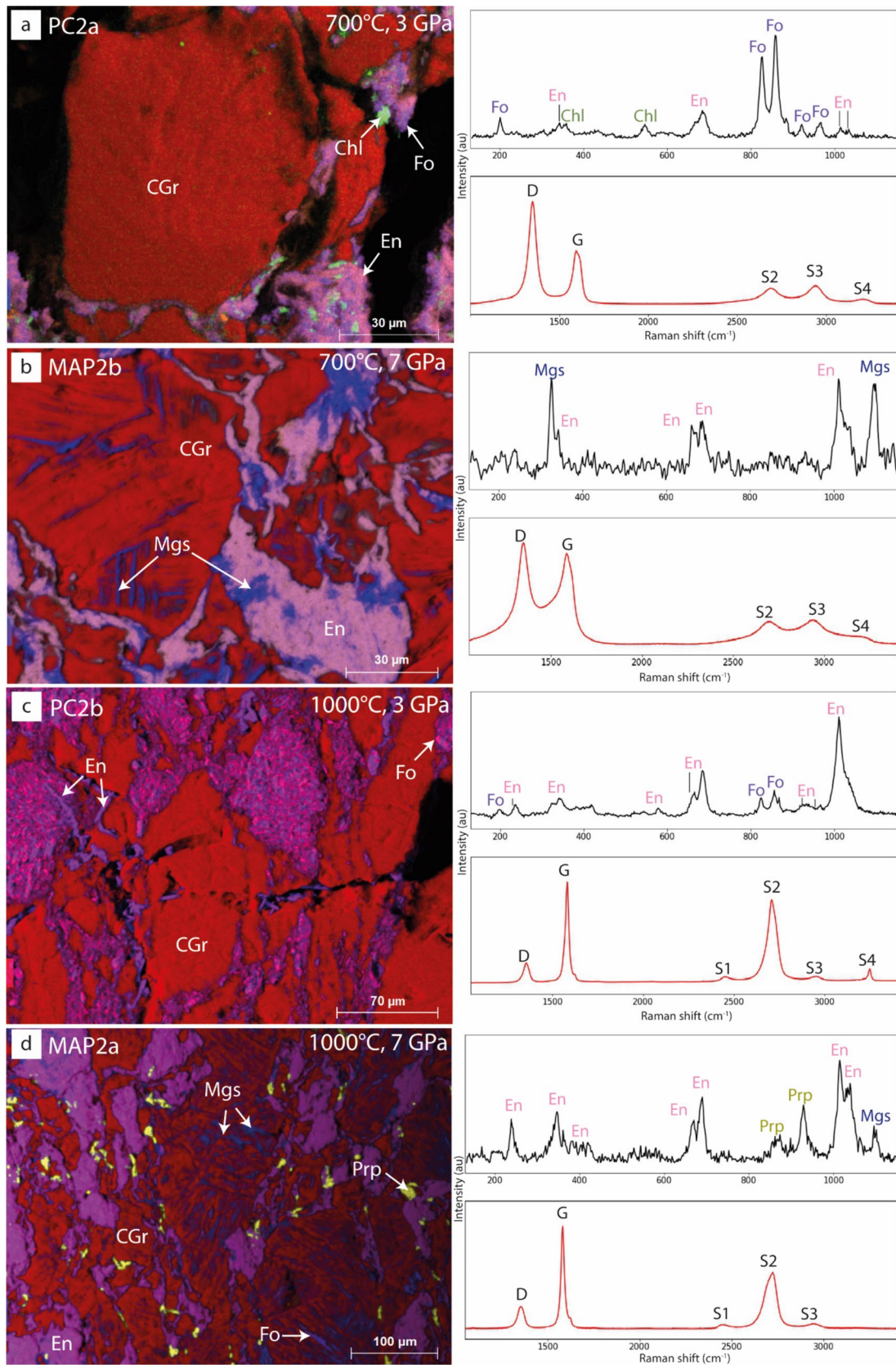
◄**Fig. 5** Composite SEM–EDS chemical maps (C (red), Mg (blue), Al (cyan), Si (yellow); left) and associated Raman spectra (right) of pyrene-antigorite mixing (50:50 by mass) PC press and MAP experiments performed at increasing P and T. **a** PC2a (700 °C, 3 GPa), **b** MAP2b (700 °C, 7 GPa), **c** PC2b (1000 °C, 3 GPa), and **d** MAP2a (1000 °C, 7 GPa; see Table 1 for associated experimental conditions and Raman D and G band parameters, as well as Fig. 2 for band assignment). Magnesite formation is only observed in the MAP experiments at 7 GPa and 700 or 1000 °C (see also Fig. 6). CGr: graphitic carbon, Chl: chlorite, En: enstatite, Fo: forsterite, Mgs: magnesite, Prp: pyrope. au: arbitrary unit

amount of garnet. Furthermore, the Al_2O_3 content is much higher in the enstatite obtained at 1000 °C than in that obtained at 700 °C (4.6 wt% at 1000 °C vs. 1.6–3.0 wt% at 700 °C), hence limiting garnet formation.

At 7 GPa and 700 °C (MAP2b; Fig. 5b), silicate assemblages are mainly composed of enstatite (around 25% of the run products) and olivine (<15% with X_{Mg} value of 0.94, comparable to the ones obtained in PC experiments at the same temperature). An aluminium-rich phase of about ~1 μm in size is observed at the center of the capsule, crystallizing between graphitic carbon layers and representing less than 2% of the capsule surface. Because of its small size, it was not possible to identify this Al-rich phase by Raman spectroscopy. Its chemical composition supports nonetheless the presence of pyrope garnet (Table S2). The Al_2O_3 content in enstatite is comparable to the one in PC experiments at 3 GPa and 700 °C (2.8 wt% at 7 GPa vs. 1.6–3.0 wt% at 3 GPa). Magnesite ($X_{Mg} = 0.89$) is also associated with both silicates and graphitic carbon sheets (Fig. 6) and accounts for about 5–10% of the run products.

At 7 GPa and 1000 °C (MAP2a, MAP2c, MAP2e; Fig. 5d), the silicate minerals present notable differences in composition and relative proportions. Enstatite and garnet are always observed, representing respectively about 20–40% (depending on the experiment) and 5% of the run products. Enstatite Al_2O_3 content ranges from 0.3 to 1.5 wt%, which is less than at 700 °C at the same pressure (2.8 wt%). Conversely, X_{Mg} values, ranging from 0.95 to 1.00, are higher (contrarily to what is observed at 3 GPa and 1000 °C). Garnet compositions are very similar when comparing similar P–T conditions and fall between that of pyrope $MgAl_2Si_3O_{12}$ and almandine $Fe^{2+}Al_2Si_3O_{12}$ (e.g., for MAP2a: 87% pyrope vs. 13% almandine based on the chemical compositions using the Droop method, Droop 1987). Olivine and magnesite relative amounts are highly variable in the run products and X_{Mg} values of olivine are slightly higher than at 700 °C (as for 3 GPa and 1000 °C) while X_{Mg} values of magnesite are extremely higher ($X_{Mg} = 1$) in the three experiment. In MAP2e, olivine ($X_{Mg} = 0.99$) represents about 25% of the run products while magnesite is found mainly in graphitic carbon layers in very small quantities (about 5%). In MAP2a, olivine

($X_{Mg} = 0.95$) represents less than 15% of the run products and crystallized in and next to the silicate assemblages, between the graphitic carbon sheets (Fig. 5d). Magnesite occurs mainly in graphitic carbon but is also observed in silicate assemblages (Fig. 6) and represents up to 5–10% of the run products. In MAP2c, olivine is absent. Magnesite represents up to 30% of the run products, and crystallized both in silicate assemblages and between the graphitic carbon sheets. Moreover, coesite is also observed in this experiment, representing up to 5–10% of the run products.

We assume that local equilibrium is reached in most experiments (except in PC2b and MAP2b where garnet is not observed), as the observed silicate assemblages are in agreement with standard dehydration assemblages observed, (Ulmer and Trommsdorff 1995; Bromiley and Pawley 2003; Pawley 2003).

In all the experiments, pyrene has been replaced by graphitic carbon, variously sheeted depending on the temperature and pressure. Raman spectra show D and G bands in the first order region and S1, S2, S3 and S4 bands in the second order one (Fig. 5). As shown in Table 1 and observed with pyrene experiments, Raman parameters associated with D1 and G bands evolve significantly with temperature (e.g., at 3 GPa, between PC2a and PC2b experiments; Fig. 5a, c.) and less with pressure (e.g., at 700 °C, between PC2a and MAP2b experiments; Fig. 5a, b). For instance, at 700 °C and 3 or 7 GPa, RBS values range between 250 and 245 cm^{-1} while they fall between 225 and 228 cm^{-1} at 1000 °C and 3 or 7 GPa. Compared to the experiment performed only with pyrene, at 700 °C–3 GPa and 1000–700 °C, the RBS and G-FWHM values are equivalent for the same P–T conditions (about 250 cm^{-1} and 55 cm^{-1} at 700 °C and 3 GPa and 228 cm^{-1} and 21 cm^{-1} at 1000 °C and 7 GPa) (Table 1). R1 values are slightly different. At 700 °C and 3 GPa, R1 ratio is higher (1.95 for PC2a vs. 1.60 for PC1f) while it is lower at 1000 °C and 3 GPa (0.19 for PC2b vs. 0.65 for PC1c). At 1000 °C and 7 GPa, R1 values (0.21 and 0.55) are around the one of MAP1a (0.35).

TOF–SIMS spectra have been collected on run products of pyrene and antigorite at 1000 °C and 3 GPa (PC2b; Supplementary Fig. S4e, f; Table S1) and compared to the one obtained for pyrene at 1000 °C and 7 GPa (MAP1; Fig S4c, d; Table S1). Compared to the positive polarity TOF–SIMS spectrum of MAP1 where only short carbon and aliphatic chains are observed, the positive polarity TOF–SIMS spectrum of PC2b shows oxygen-bearing fragment ions ($C_2H_3O_2^+$, $C_4H_5O^+$). The negative polarity TOF–SIMS spectrum of both experiments are similar, the main difference being the presence of one oxygen-bearing fragment ion ($C_3H_5N_2O^-$) in PC2b.
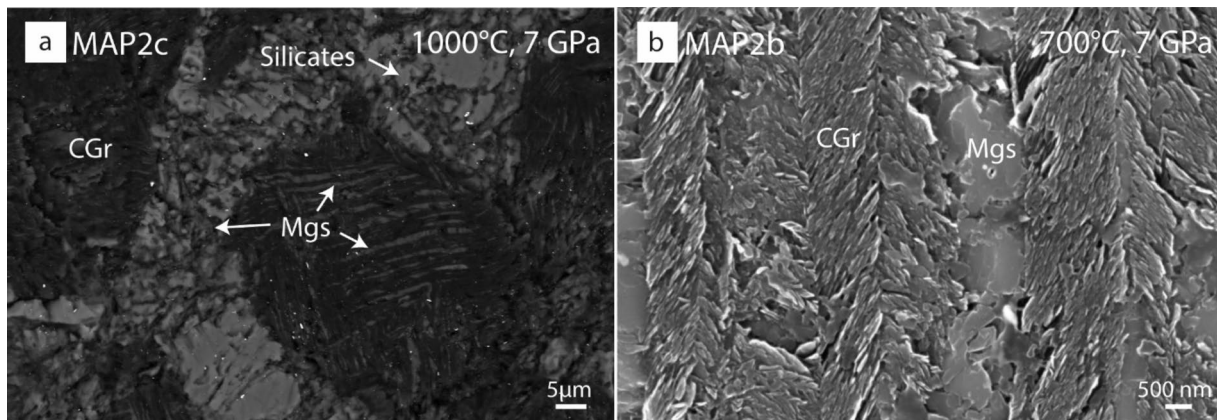
Fig. 6 Magnesite formed in MAP experiments (7 GPa, 700 and 1000 °C) involving a pyrene-antigorite mixing (50:50 by mass). **a** Orientated magnesite formation in graphitic carbon or silicates domains (SEM-BSE). **b** Interplanar magnesite formation in graphitic carbon (SEM-SE). CGr: graphitic carbon, Mgs: magnesite

Oxygen fugacity prevailing in antigorite-pyrene experiments

The oxygen fugacity can be constrained in the MAP experiments involving antigorite-pyrene mixing when either magnesite or coesite are observed in the obtained mineralogical assemblages.

In MAP2a, MAP2b, and MAP2e experiments where magnesite is present, fO_2 is calculated using the equilibrium EMOG between enstatite, magnesite, olivine (forsterite) and graphitic carbon C_{gr} (approximated to graphite):

$$\underset{Forsterite}{Mg_2SiO_4} + C_{gr} + O_2 \leftrightarrow \underset{Enstatite}{MgSiO_3} + \underset{Magnesite}{MgCO_3} \tag{1}$$

The equilibrium constant K can be expressed as:

$$ln\,K = \frac{-\Delta_r G_1^\circ(P,T)}{RT} = ln\,\frac{aMgSiO_3 \times aMgCO_3}{aMg_2SiO_4 \times aC_{gr} \times aO_2} \tag{2}$$

with $-\Delta_r G_1^\circ$, the Gibbs free energy in J mol^{-1}, P, the pressure in Pa, T, the temperature in Kelvin, R, the gas constant value and a, the activities of components. Activity of graphite is approximated to unity while the activities of enstatite, magnesite and forsterite are calculated using a Margules model with mixing on two sites (as in Holland and Powell 1998). Accordingly, activity of a specie A in a phase χ is $a_A^\chi = X_A^2 \gamma_A$ with X the mole fraction of the specie A, γ_A, the activity coefficient defined from the expression $RT\,ln\,\gamma_A = W_{A-B}^\chi X_B^2$ with and W, the Margules parameter.

Magnesite activity is only calculated at 700 °C because it is found pure at 1000 °C (its activity is then approximated to unity at this temperature). Therefore, it follows:

$$log_{10} fO_2 = \frac{\Delta_r G_1^\circ(P,T)}{RT\,ln(10)} + log_{10}\,a_{MgSiO_3} + log_{10}\,a_{MgCO_3} - log_{10}\,a_{Mg_2SiO_4} \tag{3}$$

In MAP2c experiment where coesite is present, the oxygen fugacity is calculated using the equilibrium MCEG between magnesite, coesite, enstatite and graphitic carbon (approximated to graphite):

$$\underset{Enstatite}{MgSiO_3} + C_{gr} + O_2 \leftrightarrow \underset{Magnesite}{MgCO_3} + \underset{Coesite}{SiO_2} \tag{4}$$
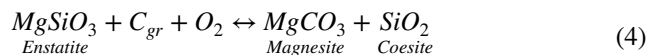
Yet again, activity of coesite and magnesite are approximated to unity as theses phases are found pure in composition while activity of enstatite is calculated as for EMOG equilibrium, so it follows:

$$log_{10} fO_2 = \frac{\Delta_r G_2^\circ(P,T)}{RT\,ln(10)} - log_{10}\,a_{MgSiO_3} \tag{5}$$

Gibbs free energies G_1° and G_2° for reactions (1) and (4), respectively, are calculated using the thermodynamic parameters provided in Supplementary Table S3. The calculated oxygen fugacities are presented in Table 3. Oxygen fugacity values are also given as ΔQFM. The quartz-fayalite-magnetite QFM buffer is calculated at 7 GPa and 700/1000 °C using the formulation of QFM provided by Ballhaus et al. (1991) and O'Neill (1987) and the data from Holland and Powell (1998), available in Maurice et al. (2020) (see Table 3).

Table 3 Estimated redox conditions during MAP experiments with associated experimental conditions, redox buffer used for calculations, and absolute and ΔQFM fO₂ values

Experiment	P (GPa)	T (°C)	Redox buffer	$log_{10} fO_2$	ΔQFM
MAP2b	7	700	EMOG	−13.54	−3.03
MAP2a, MAP2e	7	1000	EMOG	−8.45	−2.38
MAP2c	7	1000	MCEG	−7.31	−1.24

ΔQFM = log_{10}fO₂ (experiment) − log_{10}fO₂ (QFM), with log_{10}fO₂ (QFM) = 82.75 + 0.00484 T − 30,681/T − 24.45 log_{10}T + 940 P/T − 0.02 P, with T in Kelvin and P in GPa (O'Neill 1987; Maurice et al. 2020)

Discussion

P–T evolution of pyrene and two oxygen-functionalized PAHs is studied in order to assess the fate of abiotic solid organic compounds in subduction zones. These compounds were chosen since their structure and chemistry are comparable to those of abiotic CCM observed in abyssal (Andreani and Ménez 2019; Sforna et al. 2018; Andreani et al. 2023) and subduction zone (Nan et al. 2020; Debret et al. 2022) serpentinites. Low molecular weight PAHs such as pyrene and anthracene are also commonly used as simple analogues of abiotic carbonaceous matter of hydrothermal origin for thermodynamic calculations (e.g., Milesi et al. 2016; Andreani et al. 2023). Here, we first discuss the evolution of PAHs under subduction P–T conditions, and then the influence of serpentinite dehydration reactions on the metastability of PAHs.

PAHs graphitization under subduction P–T conditions

With increasing P–T conditions, pyrene Raman spectra evolve, in the first order region, from four sharp main bands at 1240, 1405, 1593 and 1626 cm^{-1} (Supplementary Fig. S3) to two broad D and G bands at about 1350 and 1600 cm^{-1} (Fig. 2e, f; Table 1) showing that the starting material turns into graphitic carbon. Graphitization can proceed through either oxidation, pyrolysis and dehydrogenation reactions (Zolotov and Shock 1999), all impacting the PAH carbon redox state of PAHs and hence their stability. Chanyshev et al. (2015, 2017a; b) already investigated pyrene graphitization with increasing P–T conditions (from 3 to 9 GPa, and 200 to 1000 °C) and propose that decomposition of PAHs is mainly controlled by condensation and dehydrogenation reactions of benzene rings into graphitic carbon. Although investigated P–T conditions are different here, we observe identical Raman spectra evolution with increasing P–T conditions, suggesting similar mechanisms affecting pyrene.

By comparing the Raman spectra of PC1f (700 °C, 3 GPa), PC1c (1000 °C, 3GPa) and MAP1a (1000 °C, 7 GPa) (Fig. 2e) and associated derived parameters, temperature seems to be the main parameter controlling PAHs graphitization while pressure has a reduced effect. Indeed, large differences in the Raman parameters are observed at 3 GPa between 700 and 1000 °C (RBS and G-FWHM values decrease from 251 to 228 cm^{-1} and 54 to 22 cm^{-1}, respectively; Table 1) while there is little difference at 1000 °C between 3 and 7 GPa (RBS = 228 cm^{-1} at both P conditions; G-FWHM values decreases from 22 to 20 cm^{-1}) regardless of the duration

of the experiment (Table 1). Similar conclusions are also drawn by Chanyshev et al. (2015), who performed HP-HT experiments using various PAHs (pyrene, naphthalene, acenaphthene $C_{12}H_{10}$, phenanthrene $C_{14}H_{10}$, fluoranthene $C_{16}H_{10}$, benzo[a]pyrene $C_{20}H_{12}$ and coronene $C_{24}H_{12}$) at 16 GPa/25 °C and 7 GPa/500–600 °C. Overall, no pure graphite formation from PAHs is reported here or in previous experiments at similar P–T conditions (Chanyshev et al. 2015, 2017a; b). Davydov et al. (2004) report the formation of pure graphite above 1200 °C from different PAHs (i.e., naphthalene, anthracene, pentacene $C_{22}H_{14}$, perylene $C_{20}H_{12}$, and coronene), hence well above the temperatures investigated here. It is interesting to note that investigations on graphitization from natural samples predict the formation of pure graphite from kerogen at temperature close to 700 °C (Beyssac et al. 2002). The persistence of a large structural disorder in the graphitic carbon obtained in experiments involving PAHs and performed below 1200 °C can be attributed either to kinetics effects associated with the experimental settings and/or to the non-graphitizable nature of the material (Beyssac and Rumble 2014; Franklin 1951).

Possible kinetic effects were tested through a series of experiments of different durations (from 1 to 7 days) performed at 700 °C and 3 GPa (Fig. 2f; Table 1). It should be noted that kinetics experiments aim at testing the graphitic carbon meta-stability, as high activation energies and kinetic factors limit comparisons between laboratory experiments and natural graphitization (Buseck and Beyssac 2014). For all these experiments, the Raman parameters of the obtained graphitic carbon do not significantly evolve, suggesting a similar structural state (RBS, G-FWHM and R1 values all in the range 250–252 cm^{-1}, 52–56 cm^{-1}, and 1.54–1.88, respectively; Table 1). Moreover, Davydov et al. (2004) report Raman spectrum of naphthalene after 60 s at 8 GPa and 1000 °C, which is very similar to the one obtained here for pyrene after 72 h at 1000 °C and 7 GPa (RBS = 223 cm^{-1} for naphtalene vs. 228 cm^{-1} here for pyrene). Overall, this suggests that the obtained graphitic carbon is at meta-equilibrium. Previous studies have shown that pressure accelerates graphitization in laboratory experiments, facilitating graphite formation at temperature of about 1000 °C from graphitizable materials (Beyssac et al. 2003 and reference therein). Hence, the preservation of a high level of disorder in pyrene-derived graphitic carbon at 1000 °C suggest pyrene is a non-graphitizable material. This disorder is likely due to the persistence of H atoms in its structure, as supported by TOF–SIMS analyses (Fig. 3a; Fig. S3a, c–d).

Both oxygen-functionalized PAHs namely 1-hydroxypyrene and PyBA show Raman spectra evolution identical to that of pyrene with increasing pressure and temperature (for instance at 700 °C and 3 GPa, RBS and G-FWHM values

are all in the range 250–251 cm^{-1} and 54–55 cm^{-1}, respectively; Table 1; Fig. 3a). Hence, the presence of oxygen does not appear to influence the graphitization level of PAHs. It must however be noted that the investigated PAHs contain heteroatoms only in the form of substituted oxygen-bearing functions. These are more easily removable than the O-bearing heterocycles potentially included in natural CCM. Nevertheless, TOF–SIMS data (Figs. 3c, 4c; Supplementary Fig. S4b) show that, in the graphitic carbon structure derived from PyBA experiment at 700 °C and 3 GPa, some oxygen is preserved and is heterogeneously distributed. Therefore, the high level of disorder preserved in graphitic carbon produced by oxygen-functionalized PAHs could be due to structural oxygen together with hydrogen (as observed in pyrene). Although we have not performed kinetics experiments on oxygen-functionalized PAHs, we assume that these PAHs are also non-graphitizable materials because (1) they present Raman spectra similar to those of pyrene at 1000 °C and comparable spectra evolution with increasing P–T (Fig. 3a) and (2) oxygen-bearing functions promote the non-graphitizable nature of organic compounds during subduction (Buseck and Beyssac 2014).

Interestingly, spherical cavities are observed in PC experiments using PyBA (Fig. 4a, b), the most oxygen-rich PAH investigated. As some of these are intersected by fractures (Fig. 4b), these cavities must have formed before the quench, which induces rapid decompression. The presence of round cavities formed at HP-HT and their enrichment in O relative to the bulk matrix revealed by TOF–SIMS imaging (Fig. 4c) therefore suggest the formation of an aqueous phase (H-, and O-rich) during PyBA graphitization at HP-HT. Similar observations are reported by Nakano et al. (2020) who observed the formation of water droplets during heating at temperatures < 350 °C of an analogue to precometary-organic-matter corresponding to a mixing of functionalized aliphatic and aromatic compounds. It is therefore possible to propose here a similar scenario with some oxygen-rich moieties exsolving as water during graphitization of oxygen-functionalized PAHs.

The three PAHs explored in our study, used as analogues of abiotic CCM in serpentinite (Sforna et al. 2018; Debret et al. 2022; Andreani et al. 2023), behave as non-graphitizable materials, preserving high level of disorder in the graphitic carbon they form at increasing pressure and temperature in experiments. In subduction zones, this non-graphitizable nature could allow the transfer at depths of volatiles (e.g., O, H or N), as it was shown in previous study on non-graphitizable materials (Nakamura et al. 2020). Moreover, the comparative Raman analysis of the experiments involving oxygen-functionalized PAHs and pyrene (Fig. 3a), as well as the presence of oxygen-bearing

fragment ions (Fig. 3c) and spherical cavities in the graphitic carbon obtained at 700 °C and 3 GPa in the PyBA experiment (Fig. 4a, b.), suggest a quick partial removal of oxygenated moieties from oxygen-bearing CCM with increasing temperature and pressure, certainly as aqueous water (see also Nakano et al. 2020). Overall, this suggests enhanced reactivity at shallow levels in subduction zones as well as and possible remaining-oxygen transfer to the deep mantle, as also supported by HP-HT solubility experiments carried out at 1 GPa, 550 °C with carbonaceous materials by Toffolo et al (2023).

In addition to oxygen, serpentinites are also known to play a major role in the recycling of other volatile and redox sensitive element to the deep Earth (e.g., Cannaò et al. 2020; Bouilhol et al. 2022). CCM may also preserve, if initially present, other heteroatoms such N and S and is therefore able of carrying part of the serpentinite volatile and redox budget to the deep mantle. For example, several studies report high nitrogen contents in lithologies from both abyssal (Philippot et al. 2007) or subduction contexts (>30 ppm; Pagé et al. 2018; Cannaò et al. 2020) and claim that serpentinites can therefore represent up to 60% of nitrogen fluxes to the deep Earth. Cannaò et al. (2020) also underline that HP oceanic rocks are likely to retain their nitrogen content beyond antigorite breakdown (i.e., 700 °C) suggesting that N is carried by secondary phases. It is well established that CCM has the potential to incorporate nitrogen into its structure (McCollom and Seewald 2007). Preserving heteroatoms, such as nitrogen, within solid organic compounds could potentially provide a new path for the deep nitrogen cycle.

On the P–T evolution of pyrene-antigorite mixing

During subduction, with the gradual increase in P–T conditions, serpentinites undergo successive dehydration reactions (i.e., brucite, antigorite, and chlorite breakdown) producing volatile-rich fluids (Ulmer and Trommsdorff 1995). These fluids may interact with abiotic CCM of hydrothermal origin enclosed in the serpentinites and enhance its solubility in slab-derived fluids, especially under oxidizing conditions (Debret et al. 2015; Debret and Sverjensky 2017; Duan et al. 2022; Iacovino et al. 2020; Maurice et al. 2020). Redox conditions are therefore of prime interest to constrain the fate of carbonaceous matter in subduction zones and hence, the deep carbon cycle.

As illustrated in Fig. 1, during the increase in P–T conditions, in MgO-Al$_2$O$_3$–SiO$_2$–H$_2$O (MASH) system, antigorite breaks down into forsterite, enstatite, and chlorite at 600–700 °C and 3 GPa (Ulmer and Trommsdorff 1995; Bromiley and Pawley 2003). This can be expressed as:
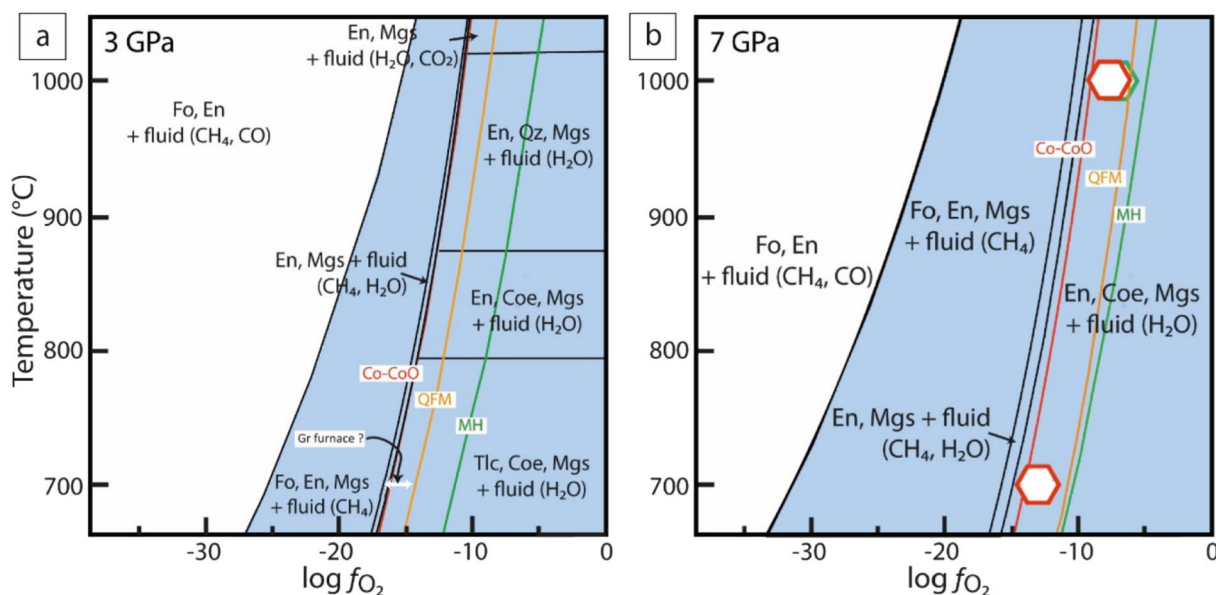
$$antigorite = forsterite + enstatite + chlorite + H_2O \qquad (6)$$

A further increase in P–T conditions, over 860 °C and 3 GPa, leads to the breakdown of chlorite releasing additional aqueous fluids (Pawley 2003) following:

$$chlorite + enstatite = pyrope + forsterite + H_2O \qquad (7)$$

In PC experiments involving a mixing of antigorite and pyrene at 700 °C and 3 GPa (PC2a, PC2d), we observe the formation of classical silicate assemblages following the breakdown of antigorite (Eq. 6), including forsterite, enstatite and chlorite (Fig. 5a; Table 1) and the breakdown of chlorite. PC experiment at 1000 °C and 3 GPa (PC2b) leads also unsurprisingly to forsterite and enstatite after chlorite breakdown (Fig. 5c; Table 1). Hence, the presence of pyrene did not influence the silicate paragenesis at HP-HT. Similarly, pyrene graphitization is not modified by dehydration reactions, at least when considering the structural evolution of the graphitic carbon formed. Raman spectra show the same graphitization level as in the pyrene experimental series (RBS and G-FWHM values are all in the range 250–251 cm^{-1} and 54–55 cm^{-1}, respectively; Table 1). However, TOF–SIMS spectra of PC2b (Supplementary Fig. S4e–f) show the presence of oxygen-bearing fragment ions which were absent in those obtained for the pyrene experiments, indicating that oxygen is incorporated into the graphitic carbon following antigorite dehydration, overall supporting potential reactivity. Nevertheless, graphitic carbon and silicates are localised in distinct areas and no graphitic carbon is observed within the silicate domains (Fig. 5a c). This suggests that pyrene is poorly solubilized in the fluid phase produced by antigorite and chlorite breakdown in PC experiments.

Conversely, in MAP experiments, in addition to classical dehydration products formed after antigorite and chlorite breakdowns, i.e., enstatite, pyrope ± forsterite (Eqs. 6 and 7; Fig. 1), the formation of magnesite is observed in all the experiments, at both 700 °C and 1000 °C. Magnesite forms in variable relative proportions both at the expense of graphitic carbon and as an interstitial phase in silicate domains (Figs. 5b, d, 6). These observations support ongoing reactions between silicate and pyrene domains leading to the oxidation of pyrene-derived organic phases into carbonates. The residual graphitic carbon shows similar graphitization levels relative to the experimental series carried out with pyrene alone (identical RBS values of 228 cm^{-1} and G-FWHM values in the range 20–27 cm^{-1}, for the experiments performed at 1000 °C and 7 GPa; Table 1). Magnesite formation can be explained by the consumption of forsterite formed by antigorite dehydration and the oxidation of graphitic carbon, expressed in the CO$_2$–MgO–SiO$_2$–H$_2$O system as:

$$\underset{Antigorite}{Mg_3Si_2O_5(OH)_4} + C_{gr} + O_2 = \underset{Magnesite}{MgCO_3} + \underset{Enstatite}{2MgSiO_3} + 2H_2O$$

$$(8)$$

The nature of the fluid, here expressed as H$_2$O will depend on the redox conditions, which are not controlled here.

Coesite is also observed in experiment MAP2c in the silicate paragenesis without forsterite suggesting competition between the two phases under these P–T conditions.

Overall, two major features emerge from the HP-HT experiments involving antigorite-pyrene mixing. Firstly, the formation of magnesite is evident in MAP experiments, whereas this phase is absent in PC experiments. Secondly, there is a variability in the silicate assemblages (i.e., presence of forsterite vs. coesite) formed at 1000 °C and 7 GPa using MAP. Both features could be explained by variable redox conditions either among MAP experiments or in between PC and MAP experiments. The influence of fO$_2$ on silicate and carbonate assemblages was approached through PerpleX pseudosections in the simplified CO$_2$–MgO–SiO$_2$–H$_2$O system at 3 and 7 GPa (Fig. 7). At low oxygen fugacity, organic carbon (represented by CH$_4$, as detailed in the "Materials and methods" section) remains stable in the presence of enstatite and forsterite. In contrast, a higher oxygen fugacity favours the formation of magnesite, either in equilibrium with olivine or coesite (in addition to enstatite), as oxygen fugacity increases. This suggests that there are variable fO$_2$ conditions either among MAP experiment and between PC and MAP experiments. PC experiments appear to be equilibrated at low oxygen fugacity in the CH$_4$-Fo-En field, whereas MAP experiments seem to be equilibrated at higher oxygen fugacity, either in the Mgs-Fo-En or the Mgs-En-Coe fields. These pseudosections show that oxygen fugacity is a critical parameter affecting the stability of carbon phases in the experiments.

This raises the question of what buffers the oxygen fugacity in both PC and MAP experiments, with fO$_2$ being either internally regulated by the newly-formed assemblages or externally controlled by the experimental device.

During experiments, antigorite dehydration products or graphitizing pyrene can internally buffer fO$_2$. The redox state and redox capacity of fluids produced by antigorite dehydration have been the subject of recent controversies (Debret and Sverjensky 2017; Merkulova et al. 2017; Bretscher et al. 2018; Piccoli et al. 2019; Iacovino et al. 2020; Maurice et al. 2020; Evans and Frost 2021; Duan et al. 2022). The presence of hematite or hemo-ilmenite in HP-HT oceanic rock samples implies that the breakdown of antigorite can produce fluids that equilibrate nearby ΔQFM +3 (Debret et al. 2015). This suggests that such fluids have the potential to oxidize graphitizing pyrene into magnesite, as observed in Fig. 6. The formation of oxidizing fluids during antigorite

Fig. 7 Phase diagram pseudosections in the CO_2–SiO_2–MgO–H_2O systems for an antigorite-pyrene mixing (50:50 by mass) at **a** 3 GPa and **b** 7 GPa plotting temperature vs. oxygen fugacity (fO_2). In both pseudosections, at low oxygen fugacity (i.e., below about −32 and −20 at 700 °C and 1000 °C, respectively), magnesite formation is not achievable. As oxygen fugacity increases, magnesite appears at the expense of forsterite, and coesite stabilises. The composition of the fluid change, from CH_4-dominated at low oxygen fugacity to H_2O-dominated at high oxygen fugacity. Polygons represent the oxygen fugacity of MAP experiments calculated based on the equilibrium EMOG buffer (red polygons for experiments MAP2a, MAP2b and MAP2e) or MCEG buffer (green polygon for experiment MAP2c) (Table 3). White arrow represents the fO_2 imposed by the PC graphite furnace based on Hermann and Spandler (2008). Cobalt-cobalt oxide (Co-CoO), quartz-fayalite-magnetite (QFM), and magnetite-hematite (MH) buffers are given for better readability. There were calculated and ploted thanks to oxygen buffer calculator Copyright © 2021 Michael Anenburg, available at: https://fo2.rses.anu.edu.au/fo2app/, consulted the 28/07/24. RRO buffer should impose fO_2 within a range of ΔQFM −1 and ΔQFM +3, between NNO and MH buffers. Light blue fields are magnesite-bearing fields. Coe: coesite, En: enstatite, Fo: forsterite, Mgs: magnesite, Qz: quartz, Tlc: talc

breakdown is attributed to the reduction of iron in serpentinites (Debret et al. 2014; 2015).

$$Fe_2O_3(s) + H_2(aq) = 2FeO(s) + 2H_2O(aq) \quad (9)$$
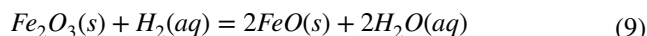
This reduction has to be coupled with the oxidation of a reduced component, which can be express in our experiment as:

$$C_{gr}(s) + H_2O(aq) = CO_2(s) + H_2(aq) \quad (10)$$
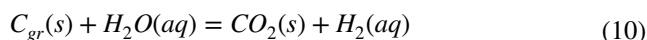
Such a redox process can therefore be expressed as:

$$2Fe_2O_{3\,antigorite} + C_{graphitizing\,pyrene} = 4FeO_{antigorite} + CO_2 \quad (11)$$
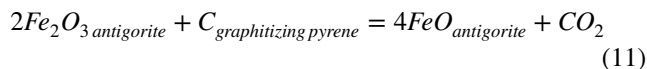
During the experiment, the oxidation of pyrene is therefore controlled by the $Fe^{3+}/\Sigma Fe$ ratio in antigorite (as magnetite has been manually removed, see "Materials and methods" section). The initial iron redox state of the antigorite used is 0.2, which corresponds to approximately 4.0 10^{-5} mol of antigorite capable of oxidizing $4.7 \cdot 10^{-3}$ mol of carbon (see Supplementary Methods for detailed calculations). This suggests that iron reduction can only account for the oxidation of less than 1% of the total carbon content

in our experiments. Consequently, this process seems to be unrealistic in explaining the large amount of magnesite observed (Fig. 6). Moreover, antigorite iron reduction cannot explain the absence of magnesite in PC experiments.

The other internal buffer of fO_2 is the graphitic carbon. In natural settings, an increasing body of literature shows occurrences of solid organic compounds under reduced conditions in subduction settings. As an example, Vitale Brovarone et al. (2017) report the formation of graphitic carbon in meta-ophicarbonates from the Lanzo Massif (Western Alps) linked to the circulation of highly reducing H_2-bearing fluids. Recently, abiotic disordered carbonaceous matter was found in meta-ophicarbonates from the Monviso meta-ophiolite (Western Alps) that recorded low fO_2 conditions (ΔQFM −4) (Caurant et al. 2023). These disordered carbonaceous compounds (Vitale Brovarone et al. 2017; Caurant et al. 2023) can lower down the fO_2 thanks to their reactivity. Indeed, due to the small size of its coherent aromatic domains and its hydrogenated character, graphitic carbon can be easily functionalized through H–O substitutions during redox changes. As heating, and hence graphitization progress, the size of the coherent domains increases and the structure dehydrogenates. It is therefore plausible

that the graphitic carbon buffer capacity decreases with increasing temperature, leading to paragenesis equilibrated at increased fO_2 (i.e., as in MAP experiments relative to PC experiments). This hypothesis was tested through experiment PC2b (1000 °C, 3 GPa), where the chlorite breakdown is reached. The absence of magnesite in this experiment rules out the role of graphitic carbon in controlling the fO_2 in our experiments, therefore calling for alternative scenarios.

An external control of oxygen fugacity might be attributed to the assembly used in the HP device, which includes the pressure medium, the thermal insulator sleeve, the furnace, the spacers and the capsule (Supplementary Fig. S1). As the present experiments are "unbuffered", i.e., the redox conditions are not imposed by a defined buffer added to the experiment (for instance using a double capsule technique e.g. Eugster and Skippen 1967), all the parts of the assembly exert an intrinsic fO_2 on the experiment. This fO_2 can be imposed to the sample by the available H_2 content in the assembly, which highly depends on the preparation of the parts (that in particular should be dried to avoid moisture) (Luth 1989; Matjuschkin et al. 2015). As a result, the intrinsic fO_2 applied to an experimental sample is very variable between studies and experiments depending on the assembly used and its preparation.

During our experiments, the MgO spacers could have buffered the fO_2 at more oxidized conditions compared to other materials (Kägi et al. 2005). However, MgO is used in both assemblies and therefore cannot explain the different mineral assemblages observed in our experiments. Similarly, capsules are made of Pt in both devices, ruling out a difference in H permeability to explain the variation in fO_2. The parts in assemblies that differ between PC press and MAP experiments are the pressure medium (talc-Pyrex in PC press vs. MgO in MAP; see Supplementary Fig. S1), the thermal insulator sleeve (again talc-Pyrex in PC press vs. LaCrO$_3$ in MAP) and the furnace (graphite in PC press vs. Re in MAP). The talc-Pyrex part (present in PC) is critical because the water released from talc dehydration increases H_2 availability and therefore the fO_2 equilibration with a buffer (which can be another part of the assembly). Pyrex can prevent H_2 diffusion during a few hours (Matjuschkin et al. 2015), sofaster equilibration of fO_2 with the different parts of the assembly is expected in PC press experiments compared to the MAP ones. LaCrO$_3$ (used in MAP) was used by Maurice et al. (2020) and was reported as to be "inert with respect to fO_2", without significant reducing or oxidizing power.

The remaining possible control on fO_2 that could explain the different mineral assemblages between the two experimental devices is the furnace, PC and MAP experiments employing graphite and rhenium furnaces, respectively.

Maurice et al. (2020) performed antigorite dehydration experiments in MAP (at 3 GPa and 600–900 °C) using either a graphite or a LaCrO$_3$ furnace. They observe the absence of hematite in graphite furnace experiments, while hematite formed in LaCrO$_3$ furnace experiments. The presence of hematite indicates fO_2 conditions beyond the magnetite-hematite (MH) redox buffer, i.e., at ΔQFM +3. In contrast, Merkulova et al. (2017), who also used a graphite furnace in their PC experiment (at 2 GPa and 600–900 °C) do not report the presence of hematite. This supports the buffering capacity of the graphite furnace, which imposes fO_2 conditions within the range ΔQFM −2 and QFM (value from Truckenbrodt et al. 1997), thereby preventing the formation of hematite. This ΔQFM range is equivalent to an absolute $\log_{10}fO_2$ ranging from −16.13 to −14.13 at 700 °C and 3 GPa. Hermann and Spandler (2008) report a similar value, close to the NNO buffer, i.e., $\log_{10}fO_2 = -14.83$ for a comparable assembly at 700 °C and 3 GPa in PC press (i.e., Teflon foil, salt outer sleeve, Pyrex glass, graphite furnace and MgO inserts) coupled with a gold capsule. It should be noted that the employing of a Pt capsule in our experiments rather than a gold one should accelerate the equilibration of fO_2 at the value imposed by the furnace as platinum has an higher permeability to H_2 than gold (Jakobsson 2012; Chou 1986).

In our experiments, the buffering capacity of the graphite furnace in PC press can therefore prevent magnesite formation. Conversely, the rhenium furnace used in MAP experiments does not have the same buffering capacity, potentially allowing an increase in oxygen fugacity during serpentine dehydration. Indeed, the rhenium furnace, as well as rhenium oxides (i.e. RRO buffer) should impose fO_2 within the range ΔQFM −1 and ΔQFM +3, between NNO and MH buffers (nonetheless extrapolated from high temperature low pressure conditions in Pownceby and O'Neill 1994). This could explain the formation of magnesite and the alternating presence of coesite or forsterite in MAP experiments. By comparing PerpleX calculations with fO_2 estimates for PC experiments (using values from Truckenbrodt et al. 1997) (Fig. 7), it must be noted that the estimated range of fO_2 values (from −16.13 to −14.13) should theoretically allow magnesite appearance. Such a disagreement might be attributed to simplifications with thermodynamic modelling or neglecting organic compounds other than graphite and methane. It is also possible that the relative amount of magnesite predicted in thermodynamic modelling calculations is too low (less than 1%) to be readily observed.

In MAP experiments, the $\log_{10}fO_2$ values calculated after EMOG (−13.54 at 700 °C or ΔQFM −3.03; −8.45 at 1000 °C or ΔQFM −2.38) and MCEG (−7.31 or ΔQFM −1.24) buffers are in the magnesite stability fields (Fig. 7; Table 3). However, based on the PerpleX predictions at 7 GPa, these values are also in the coesite stability field

while only one experiment presents the correct equilibrated mineral assemblage (i.e., MAP2c; Table 1). This could be attributed to slight variations in the relative proportions of antigorite vs. pyrene in the starting materials (see "Materials and methods" section). A high carbon concentration will favour the stabilization of coesite relative to forsterite (see Supplementary Fig. S5). The formation of magnesite in these experiments occurs below ΔQFM -2, suggesting that oxygen fugacity is even lower in PC experiments where magnesite is not observed.

In natural settings, several studies have highlighted large fO$_2$ variations within subducting slabs, ranging from ΔQFM -4 to ΔQFM $+4$ (Debret and Sverjensky 2017; Merkulova et al. 2017; Bretscher et al. 2018; Piccoli et al. 2019; Iacovino et al. 2020; Maurice et al. 2020; Evans and Frost 2021; Duan et al. 2022). This variability can be attributed to the protolith, notably the redox state and budget of abyssal serpentinites (Bretscher et al. 2018; Evans and Frost 2021), as well as other slab components, such as sediments (Caurant et al. 2023; Padrón-Navarta et al. 2023). In particular, the reaction between carbonated lithologies and serpentinite-derived fluids is likely to produce reducing conditions (Galvez et al. 2013; Vitale Brovarone et al. 2017; Caurant et al. 2023; Maffeis et al. 2023; Eberhard et al. 2023), while the redox impact of the organic carbon counterpart during serpentinite dehydration is unknown. While thermodynamic modelling allow to predict the stability of organic compounds in fluids under reducing conditions (Sverjensky et al. 2014), we show here with our experimental approach that under such reducing conditions, solid organic carbon is unlikely to react with serpentine-derived fluids and tends to remain metastable within the dehydrated silicate assemblages. As graphitization progresses, the size of its coherent domains increases and its structure dehydrogenates, hence leading to decreased reactivity with increasing temperature for the graphitic carbon. This limited reactivity likely restrains carbon solubility and mobility in fluids. This ligns with Szlachta et al. (2022) who observed the decomposition of aqueous acetate ions into graphitic carbon at 5 GPa and 600 °C, calling for carbon metastability as a solid rather than in the fluid phase. Overall, this shows that, under reducing conditions, solid organic compounds are retained in HP-HT parageneses, thus limiting carbon transfer to the mantle wedge and promoting their recycling into the deep mantle. In contrast, serpentinite dehydration under oxidizing conditions seems to oxidize graphitic carbon, resulting in the formation of oxidized carbonate ions in fluids, as evidenced by the presence of magnesite within silicate domains in our experiments (Figs. 5, 6). Hence, significant transfer of carbon from the slab to the mantle could be limited by an increase of oxygen fugacity within the slab during prograde metamorphism. This decoupling behaviour of carbon was recently reported for natural rocks by Bouilhol et al. (2022) who highlight the presence of carbonates in HP metamorphic veins and the presence of various types of graphitic carbon in the residual dehydrated serpentinites. Therefore, beyond the encountered P–T conditions, it is the redox reaction pathway of metamorphic rocks that becomes of primary interest in better understanding the fate of carbon during subduction.

Conclusion

HP-HT experiments have been performed using three types of solid PAHs, with some containing oxygen-bearing functional groups. These PAHs served as analogues for hydrothermal abiotic CCM increasingly reported in oceanic rocks. The experiments were conducted along a subduction gradient ranging from 700 to 1000 °C and 3 to 7 GPa. Despite different P–T conditions, we find, as previously reported, similar structural evolution of PAHs with increasing pressure and temperature, leading to the formation of graphitic carbon showing nonetheless various chemistry affecting its O and H contents. It therefore preserves a high structural disorder far from pure graphite structure, which makes it potentially reactive as subduction progresses. Moreover, aqueous fluid seems to be released from one oxygen-functionalized PAH type at low P–T conditions (700 °C, 3 GPa).

Experiments with mixing of pyrene and natural antigorite powders have reproduced the prograde dehydration reactions occurring in CCM-hosting serpentinites, i.e., antigorite and chlorite breakdown (700–1000 °C, 3–7 GPa). Depending on the experimental device used, various mineral assemblages were stabilized. In PC experiments, a conventional silicate assemblage following antigorite breakdown is observed, consisting of forsterite, enstatite, chlorite preserving graphitic carbon derived from PAH graphitization. In contrast, MAP experiments yielded an unconventional assemblage, consisting of enstatite, garnet, coesite, and magnesite. Thermodynamic calculations show that these differences can be explained by the redox conditions, likely induced by the experimental device as previously observed (Maurice et al. 2020). Under reduced conditions, CCM would be poorly reactive during serpentinite dehydration, leading to its recycling into the deep mantle. In contrast, more oxidizing conditions allow carbonate formation, potentially facilitating the transport of carbon to the mantle wedge. Thus, it appears that redox conditions are the main parameter controlling the metastability of PAHs and CCM in subduction context with potentially a large impact on the deep carbon cycle.

Declarations

Conflict of interest The authors declare that they have no known competing financial interests or personal relationships that could have appeared to influence the work reported in this paper.

References

Ague JJ, Nicolescu S (2014) Carbon dioxide released from subduction zones by fluid-mediated reactions. Nat Geosci 7:355–360. https://doi.org/10.1038/ngeo2143

Andreani M, Ménez B (2019) New perspectives on abiotic organic synthesis and processing during hydrothermal alteration of the oceanic Lithosphere. In: Orcutt BN, Daniel I, Dasgupta R (eds) Deep carbon: past to present, 1st edn. Cambridge University Press, Cambridge, pp 447–479

Andreani M, Montagnac G, Fellah C, Hao J, Vandier F, Daniel I, Pisapia C, Galipaud J, Lilley M, Früh Green G, Borensztajn S, Ménez B (2023) The rocky road to organics needs drying. Nat Commun 14:347. https://doi.org/10.1038/s41467-023-36038-6

Ballhaus C, Berry RF, Green DH (1991) High pressure experimental calibration of the olivine-orthopyroxene-spinel oxygen geobarometer: implications for the oxidation state of the upper mantle. Contrib Mineral Petrol 107:27–40. https://doi.org/10.1007/bf00311183

Beny-Bassez C, Rouzaud JN (1984) Characterization of carbonaceous materials by correlated electron and optical microscopy and Raman microspectroscopy. Scanning Electron Microsc 1985:119–132

Beyssac O, Rumble D (2014) Graphitic carbon: a ubiquitous, diverse, and useful geomaterial. Elements 10:415–420. https://doi.org/10.2113/gselements.10.6.415

Beyssac O, Goffé B, Chopin C, Rouzaud JN (2002) Raman spectra of carbonaceous material in metasediments: a new geothermometer. J Metamorph Geol 20:859–871. https://doi.org/10.1046/j.1525-1314.2002.00408.x

Beyssac O, Brunet F, Petitet J-P, Goffe B, Rouzaud J-N (2003) Experimental study of the microtextural and structural transformations of carbonaceous materials under pressure and temperature. Eur J Mineral 15:937–951. https://doi.org/10.1127/0935-1221/2003/0015-0937

Blanchard I, Badro J, Siebert J, Ryerson FJ (2015) Composition of the core from gallium metal–silicate partitioning experiments. Earth Planet Sci Lett 427:191–201. https://doi.org/10.1016/j.epsl.2015.06.063

Bose K, Navrotsky A (1998) Thermochemistry and phase equilibria of hydrous phases in the system MgO–SiO_2–H_2O: implications for volatile transport to the mantle. J Geophys Res 103:9713–9719. https://doi.org/10.1029/98JB00506

Bouilhol P, Debret B, Inglis EC, Warembourg M, Grocolas T, Rigaudier T, Villeneuve J, Burton KW (2022) Decoupling of inorganic and organic carbon during slab mantle devolatilisation. Nat Commun 13:308. https://doi.org/10.1038/s41467-022-27970-0

Bretscher A, Hermann J, Pettke T (2018) The influence of oceanic oxidation on serpentinite dehydration during subduction. Earth Planet Sci Lett 499:173–184. https://doi.org/10.1016/j.epsl.2018.07.017

Bromiley GD, Pawley AR (2003) The stability of antigorite in the systems MgO–SiO_2–H_2O (MSH) and MgO–Al_2O_3–SiO_2–H_2O (MASH): the effects of Al^{3+} substitution on high-pressure stability. Am Mineral 88:99–108. https://doi.org/10.2138/am-2003-0113

Buseck PR, Beyssac O (2014) From organic matter to graphite: graphitization. Elements 10:421–426. https://doi.org/10.2113/gselements.10.6.421

Bustin RM (1995) Mechanisms of graphite formation from kerogen: experimental evidence. Int J Coal Geol 8:1–36. https://doi.org/10.1016/0166-5162(95)00002-U

Cannaò E, Tiepolo M, Bebout GE, Scambelluri M (2020) Into the deep and beyond: carbon and nitrogen subduction recycling in secondary peridotites. Earth Planet Sci Lett 543:116328. https://doi.org/10.1016/j.epsl.2020.116328

Carignan J, Hild P, Mevelle G, Morel J, Yeghicheyan D (2001) Routine analyses of trace elements in geological samples using flow injection and low pressure on-line liquid chromatography coupled to ICP-MS: a study of geochemical reference materials BR, DR-N, UB-N, AN-G and GH. Geostand Newslett 25:187–198. https://doi.org/10.1111/j.1751-908X.2001.tb00595.x

Caurant C, Debret B, Ménez B, Nicollet C, Bouihol P (2023) Redox heterogeneities in a subducting slab: example from the Monviso meta-ophiolite (Western Alps, Italy). Lithos 446–447:107136. https://doi.org/10.1016/j.lithos.2023.107136

Chanyshev AD, Litasov KD, Shatskiy AF, Furukawa, Yoshino T, Ohtani E (2015) Oligomerization and carbonization of polycyclic aromatic hydrocarbons at high pressure and temperature. Carbon 84:225–235. https://doi.org/10.1016/j.carbon.2014.12.011

Chanyshev AD, Litasov KD, Furukawa Y, Kokh KA, Shatskiy A (2017a) Temperature-induced oligomerization of polycyclic aromatic hydrocarbons at ambient and high pressures. Sci Rep 7:7889. https://doi.org/10.1038/s41598-017-08529-2

Chanyshev AD, Litasov KD, Shatskiy AF, Sharygin IS, Higo Y, Ohtan E (2017b) Transition from melting to carbonization of naphthalene, anthracene, pyrene and coronene at high pressure. Phys Earth Planet Inter 270:29–39. https://doi.org/10.1016/j.pepi.2017.06.011

Chou I-M (1986) Permeability of precious metals to hydrogen at 2 kb total pressure and elevated temperatures. Am J Sci 286:638–658. https://doi.org/10.2475/ajs.286.8.638

Connolly JAD (2005) Computation of phase equilibria by linear programming: a tool for geodynamic modeling and its application to subduction zone decarbonation. Earth Planet Sci Lett 236:524–541. https://doi.org/10.1016/j.epsl.2005.04.033

Connolly JAD (2009) The geodynamic equation of state: what and how. Geochem Geophys Geosyst. https://doi.org/10.1029/2009GC002540

Dasgupta R, Hirschmann MM (2010) The deep carbon cycle and melting in Earth's interior. Earth Planet Sci Lett 298:1–13. https://doi.org/10.1016/j.epsl.2010.06.039

Davydov VA, Rakhmanina AV, Agafonov V, Narymbetov B, Boudou J-P, Szwarc H (2004) Conversion of polycyclic aromatic hydrocarbons to graphite and diamond at high pressures. Carbon 42:261–269. https://doi.org/10.1016/j.carbon.2003.10.026

Debret B (2013) Serpentinites, vecteurs des circulations fluides et des transferts chimiques de l'océanisation à la subduction: exemple dans les Alpes occidentales. Dissertation, University Blaise Pascal—Clermont-Ferrand II

Debret B, Sverjensky DA (2017) Highly oxidising fluids generated during serpentinite breakdown in subduction zones. Sci Rep 7:10351. https://doi.org/10.1038/s41598-017-09626-y

Debret B, Andreani M, Muñoz M, Bolfan-Casanova N, Carlut J, Nicollet C, Schwarz S, Trcera N (2014) Evolution of Fe redox state in serpentine during subduction. Earth Planet Sci Lett 400:206–218. https://doi.org/10.1016/j.epsl.2014.05.038

Debret B, Bolfan-Casanova N, Padrón-Navarta JA, Martin-Hernandez F, Andeani M, Garrido CJ, Lopez Sanchez-Vizcaino V, Gomez-Pugnaire MT, Munoz M, Trcera N (2015) Redox state of iron during high-pressure serpentinite dehydration. Contrib Mineral Petrol 169:36. https://doi.org/10.1007/s00410-015-1130-y

Debret B, Ménez B, Walter B, Bouquerel H, Bouilhol P, Mattielli N, Pisapia C, Rigaudier T, Williams HM (2022) High-pressure synthesis and storage of solid organic compounds in active subduction zones. Sci Adv 8:eabo2397. https://doi.org/10.1126/sciadv.abo2397

Droop GTR (1987) A general equation for estimating Fe^{3+} concentrations in ferromagnesian silicates and oxides from microprobe analyses, using stoichiometric criteria. Mineral Mag 51:431–435. https://doi.org/10.1180/minmag.1987.051.361.10

Duan W-Y, Li X-P, Schertl H-P, Willner AP (2022) C-O–H–S fluids released by oceanic serpentinite in subduction zones: implications for arc-magma oxidation. Earth Planet Sci Lett 594:117709. https://doi.org/10.1016/j.epsl.2022.117709

Eberhard L, Frost DJ, Plümper O (2023) Early release of H_2O during subduction of carbonated ultramafic lithologies. Contrib Mineral Petrol 178:17. https://doi.org/10.1007/s00410-023-01997-y

Eugster HP, Skippen GB (1967) Igneous and metamorphic reactions involving gas equilibria. Res Geochem 2:492–520

Evans KA, Frost BR (2021) Deserpentinization in subduction zones as a source of oxidation in arcs: a reality check. J Petrol 62:egab016. https://doi.org/10.1093/petrology/egab016

Facq S, Daniel I, Montagnac G, Cardon H, Sverjensky DA (2014) In situ Raman study and thermodynamic model of aqueous carbonate speciation in equilibrium with aragonite under subduction zone conditions. Geochim Cosmochim Acta 132:375–390. https://doi.org/10.1016/j.gca.2014.01.030

Farsang S, Louvel M, Zhao C, Mezouar M, Rosa AD, Widmer RN, Feng X, Li J, Redfern SAT (2021) Deep carbon cycle constrained by carbonate solubility. Nat Commun 12:4311. https://doi.org/10.1038/s41467-021-24533-7

Franklin RE (1951) Crystallite growth in graphitizing and non-graphitizing carbons. Proc R Soc Lond A 209:196–218. https://doi.org/10.1098/rspa.1951.0197

Frezzotti ML (2019) Diamond growth from organic compounds in hydrous fluids deep within the Earth. Nat Commun 10:4952. https://doi.org/10.1038/s41467-019-12984-y

Frezzotti ML, Selverstone J, Sharp ZD, Compagnoni R (2011) Carbonate dissolution during subduction revealed by diamond-bearing rocks from the Alps. Nature Geosci 4:703–706. https://doi.org/10.1038/ngeo1246

Fumagalli P (2004) Experimentally determined phase relations in hydrous peridotites to 6.5 GPa and their consequences on the dynamics of subduction zones. J Petrol 46:555–578. https://doi.org/10.1093/petrology/egh088

Fumagalli P, Poli S, Fischer J, Merlini M, Gemmi M (2014) The high-pressure stability of chlorite and other hydrates in subduction mélanges: experiments in the system Cr_2O_3–MgO–Al_2O_3–SiO_2–H_2O. Contrib Mineral Petrol 167:979. https://doi.org/10.1007/s00410-014-0979-5

Galvez ME, Beyssac O, Martinez I, Benzerara K, Chatduteau C, Malvoisin B, Malavieille J (2013) Graphite formation by carbonate reduction during subduction. Nature Geosci 6:473–477. https://doi.org/10.1038/ngeo1827

Gorman PJ, Kerrick DM, Connolly JAD (2006) Modeling open system metamorphic decarbonation of subducting slabs. Geochem Geophys Geosyst. https://doi.org/10.1029/2005GC001125

Guild M, Shock EL (2020) Predicted speciation of carbon in subduction zone fluids. In: Manning CE, Lin J, Mao WL (eds) Geophysical monograph series, 1st edn. Wiley, New York, pp 285–302

Henry DG, Jarvis I, Gillmore G, Stephenson M (2019) Raman spectroscopy as a tool to determine the thermal maturity of organic matter: application to sedimentary, metamorphic and structural geology. Earth Sci Rev 198:102936. https://doi.org/10.1016/j.earscirev.2019.102936

Hermann J, Spandler CJ (2008) Sediment melts at sub-arc depths: an experimental study. J Petrol 49:717–740. https://doi.org/10.1093/petrology/egm073

Holland T, Powell R (1991) A Compensated-Redlich-Kwong (CORK) equation for volumes and fugacities of CO_2 and H_2O in the range 1 bar to 50 kbar and 100–1600°C. Contr Mineral Petrol 109:265–273. https://doi.org/10.1007/BF00306484

Holland TJB, Powell R (1998) An internally consistent thermodynamic data set for phases of petrological interest. J Metamorph Geol 16:309–343. https://doi.org/10.1111/j.1525-1314.1998.00140.x

Holland T, Powell R (2003) Activity-composition relations for phases in petrological calculations: an asymmetric multicomponent formulation. Contrib Mineral Petrol 145:492–501. https://doi.org/10.1007/s00410-003-0464-z

Huang F, Daniel I, Cardon H, Montagnac G, Sverjensky DA (2017) Immiscible hydrocarbon fluids in the deep carbon cycle. Nat Commun 8:15798. https://doi.org/10.1038/ncomms15798

Huang J, Daniel I, Sverjensky DA, Cado H, Montagnac G (2023) Formation of hydrocarbons favored by high pressure at subduction zone conditions. Chem Geol 630:121489. https://doi.org/10.1016/j.chemgeo.2023.121489

Iacovino K, Guild MR, Till CB (2020) Aqueous fluids are effective oxidizing agents of the mantle in subduction zones. Contrib Mineral Petrol 175:36. https://doi.org/10.1007/s00410-020-1673-4

Jakobsson S (2012) Oxygen fugacity control in piston-cylinder experiments. Contrib Mineral Petrol 164:397–406. https://doi.org/10.1007/s00410-012-0743-7

Kägi R, Müntener O, Ulmer P, Ottolini L (2005) Piston-cylinder experiments on H_2O undersaturated Fe-bearing systems: an experimental setup approaching fO2 conditions of natural calc-alkaline magmas. Am Mineral 90:708–717. https://doi.org/10.2138/am.2005.1663

Kelemen PB, Manning CE (2015) Reevaluating carbon fluxes in subduction zones, what goes down, mostly comes up. PNAS 112:E3997–E4006. https://doi.org/10.1073/pnas.1507889112

Li Y (2016) Immiscible C–H–O fluids formed at subduction zone conditions. Geochem Perspect Lett 3:12–21. https://doi.org/10.7185/geochemlet.1702

Luth RW (1989) Natural versus experimental control of oxidation state; effects on the composition and speciation of COH fluids. Am Mineral 74(1–2):50–57

Maffeis A, Ferrando S, Connolly JAD, Frezzotti ML, Castelli D (2023) Fluid redox fingerprint of the $CaCO_3^+$ antigorite dehydration reaction in subducted metacarbonate sediments. Geosciences 13:130. https://doi.org/10.3390/geosciences13050130

Malvoisin B, Chopin C, Brunet F, Galvez ME (2012) Low-temperature wollastonite formed by carbonate reduction: a marker of serpentinite redox conditions. J Petrol 53:159–176. https://doi.org/10.1093/petrology/egr060

Manning CE, Shock EL, Sverjensky DA (2013) The chemistry of carbon in aqueous fluids at crustal and upper-mantle conditions: experimental and theoretical constraints. RIMG 75:109–148. https://doi.org/10.2138/rmg.2013.75.5

Matjuschkin V, Brooker RA, Tattitch B, Bludy JD, Stamper CC (2015) Control and monitoring of oxygen fugacity in piston cylinder experiments. Contrib Mineral Petrol 169:9. https://doi.org/10.1007/s00410-015-1105-z

Matthewman R, Martins Z, Sephton MA (2013) Type IV kerogens as analogues for organic macromolecular materials in aqueously Altered carbonaceous chondrites. Astrobiology 13:324–333. https://doi.org/10.1089/ast.2012.0820

Maurice J, Bolfan-Casanova N, Demouchy S, Chauvigne P, Schiavi F, Debret B (2020) The intrinsic nature of antigorite breakdown at 3 GPa: experimental constraints on redox conditions of serpentinite dehydration in subduction zones. Contrib Mineral Petrol 175:94. https://doi.org/10.1007/s00410-020-01731-y

McCollom TM, Seewald JS (2007) Abiotic synthesis of organic compounds in deep-sea hydrothermal environments. Chem Rev 107:382–401. https://doi.org/10.1021/cr0503660

Menzel MD, Garrido CJ, López Sánchez-Vizcaíno V (2020) Fluid-mediated carbon release from serpentinite-hosted carbonates during dehydration of antigorite-serpentinite in subduction zones. Earth Planet Sci Lett 531:115964. https://doi.org/10.1016/j.epsl.2019.115964

Merkulova MV, Muñoz M, Brunet F, Vidal O, Hattori K, Vantelon D, Trcera N, Huthwelker T (2017) Experimental insight into redox transfer by iron- and sulfur-bearing serpentinite dehydration in subduction zones. Earth Planet Sci Lett 479:133–143. https://doi.org/10.1016/j.epsl.2017.09.009

Milesi V, McCollom TM, Guyot F (2016) Thermodynamic constraints on the formation of condensed carbon from serpentinization fluids. Geochim Cosmochim Acta 189:391–403. https://doi.org/10.1016/j.gca.2016.06.006

Mimura K, Toyama S, Sugitani K (2005) Shock-induced dehydrogenation of polycyclic aromatic hydrocarbons with or without serpentine: implications for planetary accretion. Earth Planet Sci Lett 232:143–156. https://doi.org/10.1016/j.epsl.2005.01.003

Nakamura Y, Yoshino T, Satish-Kumar M (2017) An experimental kinetic study on the structural evolution of natural carbonaceous material to graphite. Am Mineral 102:135–148. https://doi.org/10.2138/am-2017-5733

Nakamura Y, Yoshino T, Satish-Kumar M (2020) Pressure dependence of graphitization: implications for rapid recrystallization of carbonaceous material in a subduction zone. Contrib Mineral Petrol 175:32. https://doi.org/10.1007/s00410-020-1667-2

Nakano H, Hirakawa N, Matsubara Y et al (2020) Precometary organic matter: a hidden reservoir of water inside the snow line. Sci Rep 10:7755. https://doi.org/10.1038/s41598-020-64815-6

Nan J, King HE, Delen G, Meirer F, Weckhuysen BM, Guo Z, Peng X, Plumper O (2020) The nanogeochemistry of abiotic carbonaceous matter in serpentinites from the Yap Trench, western Pacific Ocean. Geology 49(3):330–334. https://doi.org/10.1130/G48153.1

O'Neill H (1987) The quartz-fayalite-iron and quartz-fayalite-magnetite equilibria and the free energies of formation of fayalite (Fe_2SiO_4) and magnetite (Fe_3O_4). Am Mineral 72:67–75

Padrón-Navarta JA, Hermann J, Garrido CJ, Lopez Sanchez-Vizcaino V (2010) An experimental investigation of antigorite dehydration in natural silica-enriched serpentinite. Contrib Mineral Petrol 159:25–42. https://doi.org/10.1007/s00410-009-0414-5

Padrón-Navarta JA, López Sánchez-Vizcaíno V, Menzel MD, Gomez-Pugnaire MT, Garrido CJ (2023) Mantle wedge oxidation from deserpentinization modulated by sediment-derived fluids. Nat Geosci 16:268–275. https://doi.org/10.1038/s41561-023-01127-0

Pagé L, Hattori K, Guillot S (2018) Mantle wedge serpentinites: a transient reservoir of halogens, boron, and nitrogen for the deeper mantle. Geology 46:883–886. https://doi.org/10.1130/G45204.1

Pan D, Spanu L, Harrison B, Sverjensky DA, Galli G (2013) Dielectric properties of water under extreme conditions and transport of carbonates in the deep Earth. PNAS 110:6646–6650. https://doi.org/10.1073/pnas.1221581110

Pasteris JD (1989) In situ analysis in geological thin-sections by laser Raman microprobe spectroscopy: a cautionary note. Appl Spectrosc 43:567–570. https://doi.org/10.1366/0003702894202878

Pawley A (2003) Chlorite stability in mantle peridotite: the reaction clinochlore+enstatite=forsterite+pyrope+H_2O. Contrib Mineral Petrol 144:449–456. https://doi.org/10.1007/s00410-002-0409-y

Peng W, Zhang L, Tumiati S, Vitale Brovarone A, Hu H, Cai Y, Shen T (2021) Abiotic methane generation through reduction of serpentinite-hosted dolomite: implications for carbon mobility in subduction zones. Geochim Cosmochim Acta 311:119–140. https://doi.org/10.1016/j.gca.2021.07.033

Philippot P, Busigny V, Scambelluri M, Cartigny P (2007) Oxygen and nitrogen isotopes as tracers of fluid activities in serpentinites and metasediments during subduction. Mineral Petrol 91:11–24. https://doi.org/10.1007/s00710-007-0183-7

Piccoli F, Hermann J, Pettke T, Connolly JAD, Kempf ED, Vieira Duarte JF (2019) Subducting serpentinites release reduced, not oxidized, aqueous fluids. Sci Rep 9:19573. https://doi.org/10.1038/s41598-019-55944-8

Plank T, Manning CE (2019) Subducting carbon. Nature 574:343–352. https://doi.org/10.1038/s41586-019-1643-z

Pownceby MI, O'Neill HSC (1994) Thermodynamic data from redox reactions at high temperatures. IV. Calibration of the Re-ReOz oxygen buffer from EMF and NiO + Ni-Pd redox sensor measurements Contrib. Mineral Petrol 118(2):130–137. https://doi.org/10.1007/BF01052864

Ross JV, Bustin RM, Rouzaud JN (1991) Graphitization of high rank coals—the role of shear strain: experimental considerations. Org Geochem 17:585–596. https://doi.org/10.1016/0146-6380(91)90002-2

Schneider CA, Rasband WS, Eliceiri KW (2012) NIH Image to ImageJ: 25 years of image analysis. Nat Methods 9:671–675. https://doi.org/10.1038/nmeth.2089

Sforna MC, Brunelli D, Pisapia C, Pasini V, Malferrari D, Ménez Bénédicte (2018) Abiotic formation of condensed carbonaceous matter in the hydrating oceanic crust. Nat Commun 9:5049. https://doi.org/10.1038/s41467-018-07385-6

Siebert J, Corgne A, Ryerson FJ (2011) Systematics of metal–silicate partitioning for many siderophile elements applied to Earth's core formation. Geochim Cosmochim Acta 75:1451–1489. https://doi.org/10.1016/j.gca.2010.12.013

Sverjensky DA, Stagno V, Huang F (2014) Important role for organic carbon in subduction-zone fluids in the deep carbon cycle. Nature Geosci 7:909–913. https://doi.org/10.1038/ngeo2291

Syracuse EM, Van Keken PE, Abers GA (2010) The global range of subduction zone thermal models. Phys Earth Planet Inter 183:73–90. https://doi.org/10.1016/j.pepi.2010.02.004

Szlachta V, Vlasov K, Keppler H (2022) On the stability of acetate in subduction zone fluids. Geochem Perspect Lett 21:28–31. https://doi.org/10.7185/geochemlet.2213

Tao R, Zhang L, Tian M, Zhu J, Liu X, Liu J, Höfer HE, Stagno V, Fei Y (2018) Formation of abiotic hydrocarbon from reduction of carbonate in subduction zones: constraints from petrological

observation and experimental simulation. Geochim Cosmochim Acta 239:390–408. https://doi.org/10.1016/j.gca.2018.08.008

Tiraboschi C, Tumiati S, Sverjensky D, Pettke T, Ulmer P, Poli S (2018) Experimental determination of magnesia and silica solubilities in graphite-saturated and redox-buffered high-pressure COH fluids in equilibrium with forsterite + enstatite and magnesite + enstatite. Contrib Mineral Petrol 173:2. https://doi.org/10.1007/s00410-017-1427-0

Toffolo L, Tumiati S, Villa A, Fumagalli P, Amalfa A, Miozzi F (2023) Experimental dissolution of carbonaceous materials in water at 1 GPa and 550°C: assessing the role of carbon forms and redox state on COH fluid production and composition during forearc subduction of organic matter. Front Earth Sci 11:1013014. https://doi.org/10.3389/feart.2023.1013014

Touboul D, Kollmer F, Niehuis E et al (2005) Improvement of biological time-of-flight-secondary ion mass spectrometry imaging with a bismuth cluster ion source. J Am Soc Mass Spectrom 16:1608–1618. https://doi.org/10.1016/j.jasms.2005.06.005

Truckenbrodt J, Ziegenbein D, Johannes W (1997) Redox conditions in piston-cylinder apparatus; the different behavior of boron nitride and unfired pyrophyllite assemblies. Am Mineral 82:337–344. https://doi.org/10.2138/am-1997-3-412

Tuinstra F, Koenig JL (1970) Raman spectrum of graphite. J Chem Phys 53:1126–1130. https://doi.org/10.1063/1.1674108

Tumiati S, Tiraboschi C, Sverjensky DA, Pettke T, Ulmer P, Miozzi F, Poli S (2017) Silicate dissolution boosts the CO_2 concentrations in subduction fluids. Nat Commun 8:616. https://doi.org/10.1038/s41467-017-00562-z

Tumiati S, Tiraboschi C, Miozzi F, Vitale-Brovarone A, Manning CE, Sverjensky DA, Milani S, Poli S (2020) Dissolution susceptibility of glass-like carbon versus crystalline graphite in high-pressure aqueous fluids and implications for the behavior of organic matter in subduction zones. Geochim Cosmochim Acta 273:383–402. https://doi.org/10.1016/j.gca.2020.01.030

Ulmer P, Trommsdorff V (1995) Serpentine stability to mantle depths and subduction-related magmatism. Science 268:858–861. https://doi.org/10.1126/science.268.5212.858

Vitale Brovarone A, Martinez I, Elmaleh A, Compagnoni R, Chatudeau C, Ferraris C, Estève I (2017) Massive production of abiotic methane during subduction evidenced in metamorphosed ophicarbonates from the Italian Alps. Nat Commun 8:14134. https://doi.org/10.1038/ncomms14134

Wopenka B, Pasteris JL (1993) Structural characterization of kerogens to granulite-facies graphite: applicability of Raman microprobe spectroscopy. Am Mineral 78:533–577

Wunder B, Schreyer W (1997) Antigorite: high-pressure stability in the system MgO–SiO_2–H_2O (MSH). Lithos 41:213–227. https://doi.org/10.1016/S0024-4937(97)82013-0

Zeng Y, Wu C (2007) Raman and infrared spectroscopic study of kerogen treated at elevated temperatures and pressures. Fuel 86:1192–1200. https://doi.org/10.1016/j.fuel.2005.03.036

Zhu J, Zhang L, Tao R, Fei Y (2020) The formation of graphite-rich eclogite vein in S.W. Tianshan (China) and its implication for deep carbon cycling in subduction zone. Chem Geol 533:119430. https://doi.org/10.1016/j.chemgeo.2019.119430

Zolotov M, Shock E (1999) Abiotic synthesis of polycyclic aromatic hydrocarbons on Mars. J Geophys Res 104:14033–14049. https://doi.org/10.1029/1998JE000627